https://doi.org/10.1016/j.engstruct.2021.113111

Experimental and numerical study on net section resistance of high strength steel staggered bolted connections

Xue-Mei Lin[a,b], Michael C.H. Yam[a,b,*], Kwok-Fai Chung[b,c], Ke Ke[d], Qun He[a,b]

[a] *Department of Building and Real Estate, The Hong Kong Polytechnic University, Hong Kong, China*
[b] *Chinese National Engineering Research Centre for Steel Construction (Hong Kong Branch), The Hong Kong Polytechnic University, Hong Kong, China.*
[c] *Department of Civil and Environmental Engineering, The Hong Kong Polytechnic University, Hong Kong, China*
[d] *Key Laboratory of New Technology for Construction of Cities in Mountain Area, School of Civil Engineering, Chongqing University, Chongqing, China*
[*] *Corresponding author. E-mail address: michael.yam@polyu.edu.hk*

Abstract

This paper investigates the structural behaviour and ultimate strength of high strength steel (HSS) staggered bolted connections under tension. A total of 33 HSS (Q690 and Q960) and 15 Q345 staggered bolted connection specimens were tested. All specimens failed in net section fracture through the staggered path. The predicted net section resistance based on the $s^2/4g$ rule was achieved by most of the HSS specimens. For the specimens with a small bolt pitch to gauge (s/g) ratio, the connection efficiency (i.e., the ratio between the test ultimate load and the calculated net section resistance) exceeded 1.0 and decreased gradually with an increasing s/g ratio. Compared with the mild steel (MS) specimens, in general the HSS specimens have lower connection efficiency and overall deformation capability. Subsequently, the structural behaviour of the test specimens was investigated using finite element (FE) analysis to further interpret the test observations. The results of the test and the FE analysis indicated that for the HSS specimens, effective stress redistribution along the staggered net section was observed although the ductility and the ratio of tensile strength to yield strength (f_u/f_y) of HSS material are relatively lower than those of the MS material. In addition, it was also observed that the biaxial state of stress that existed in the plate area between the staggered bolt holes was influenced by the *s/g* ratio, which would affect the ultimate strength of the test specimens. A reliability analysis of the HSS specimens test results was carried out to re-evaluate the partial factor adopted in the design equation of the net section resistance of HSS (up to S700) in EN 1993-1-12. The analysis results of the limited test data showed that the net section resistance of HSS staggered bolted connections was predicted conservatively by the current design equation with a partial factor of 1.25.

Keywords: High strength steel, Staggered bolted connections, Net section resistance, Reliability analysis, Finite element analysis, Experimental investigation

1. Introduction

Due to the high strength-to-weight ratio of high strength steel (HSS) material, HSS structural members are usually smaller in section size with lighter self-weight than those made using mild steel (MS) [1]. Hence, practical application of HSS in civil engineering structures can bring substantial economic and environmental benefits. For the design of HSS connections, additional design rules for steel grade up to S700 were introduced in EN 1993-1-12 in 2007 [2]. For a bolted connection under tension, an effective stress redistribution along the net section is of paramount importance for the full development of tensile strength of the material before fracture at the bolt hole. In EN 1993-1-12 [2], the net section resistance of HSS (S460~S700) section under tension is

$$N_{t,Rd} = \frac{0.9A_{net}f_u}{\gamma_{M12}} \tag{1}$$

where γ_{M12} is the partial factor for net section resistance of HSS up to S700 and is equal to 1.25, A_{net} is the net section area of HSS member, and f_{u} is the tensile strength of HSS material. For HSS bolted connections without a staggered pattern and failed in transverse net section fracture, it was found that the connections could achieve the net section resistance ($A_{\mathrm{net}}f_{\mathrm{u}}$) [3-6]. This could be attributed to the sufficient redistribution of the stress along the transverse net section [6] and the beneficial effect of biaxial stress state in the main plate [7-9]. The biaxial stress state at typical areas (i.e., $\mathrm{R}_1 \sim \mathrm{R}_3$) observed in a previous study [6] was briefly illustrated in Fig. 1, where S_{x} and S_{y} are the axial and lateral tensile stresses, respectively. The lateral tensile stress S_{y} was caused by the fact that the material in the net section area could not freely contract laterally due to the presence of bolt holes on the perforated plate under tension [10]. According to the distortion energy criterion, the biaxial stress state in Fig. 1 could lead to an increase in S_{x} in order to reach the corresponding tensile strength in contrast to the same material under uniaxial tension [10, 11].

Staggered bolt arrangement of connection is commonly adopted in structural steel design aiming to obtain the greatest possible usable area in a connection [12]. For a staggered bolted connection under tension, the biaxial stress state may also exist across the staggered net section. The net area of a staggered section is commonly determined by the $s^2/4g$ rule, where s is the pitch, and g is the gauge [13], and it has been widely adopted in the current design codes [14-17]:

$$A_{net} = t\left(W - n_s d_0 + \sum \frac{s^2}{4g}\right) \qquad (2)$$

where t and W are the thickness and the gross section width of the tension member, respectively, d_0 is the bolt hole diameter, and n_s is the number of bolts in the staggered path across the section. In recent decades, many studies have been conducted to examine the accuracy of the $s^2/4g$ rule for evaluating the net section resistance of tension members with staggered bolts. Epstein and Gulia [18] suggested that for MS staggered bolted connections, the $s^2/4g$ rule might not always provide a conservative prediction of the net section resistance. Wei *et al*. [19] tested 27 staggered bolted connections made using materials with yield strength up to 265 MPa and suggested that the $s^2/4g$ rule underestimated the net section resistance of the specimens. On the other hand, Teh and Clements [20] and Cho *et al.* [21] found that the $s^2/4g$ rule overestimated the net section resistance of the test specimens made using cold-reduced steel, such as G450. There seems to be an inconsistency among these research findings, which were based on connection specimens made using different steel materials. Recently, Jiang *et al*. [22] tested 15 high strength steel (S700) bolted connections which were failed in the staggered net section fracture mode. It was found that the bolt pattern across the staggered net section could affect the prediction accuracy of the $s^2/4g$ rule. However, the effect of material ductility on the development of staggered net section resistance was not further investigated. It is worth noting that the ductility and the ratio of the tensile strength (f_u) to the yield strength (f_y) of the material, i.e., f_u/f_y ratio of HSS material are generally lower than those of MS material [23, 24]. These material properties of HSS may affect the effective stress redistribution along the staggered net section, which may consequently reduce the tensile capacity of the connection. The authors have conducted a preliminarily numerical study of HSS staggered bolted connections, and found that the $s^2/4g$ rule could predict the corresponding net section resistance with reasonable accuracy [25].

The above discussions illustrated that there is a limited number of experimental studies of the effects of ductility and f_u/f_y ratio on the net section resistance of HSS staggered bolted connections. Therefore, this study aims at investigating experimentally the ultimate capacity of HSS staggered bolted connections. A finite element (FE) analysis of the test specimens was subsequently conducted for interpreting the test observations and providing further insights. Besides, the accuracy of the $s^2/4g$ rule was re-examined. Finally, the applicability of the current design equation of net section resistance in EN 1993-1-12 [2] to HSS staggered bolted connections was re-evaluated via a reliability analysis based on the experimental data from the current study and Jiang *et al.* [22].

2. Experimental investigation

2.1 Test specimens

48 staggered bolted connection specimens including 33 HSS and 15 MS specimens under double shear were tested to fracture. All the specimens were designed to have a transverse net section area larger than that of the staggered net section to ensure that the specimens would fail in the net section fracture mode through the staggered path. The study investigated three Chinese steel grades, namely, Q345, Q690 and Q960 with nominal yield/tensile strengths of 345/470 MPa, 690/770 MPa and 960/980 MPa, respectively [26, 27]. The elongation at fracture of Q345, Q690 and Q960 steel is no less than 22%, 14% and 10%, respectively [26, 27]. The detailed geometric configuration of the specimens and the geometric parameters such as the width of steel plate (W), end distance (e_1), edge distance (e_2), bolt hole diameter (d_0), pitch (s), gauge (g), and the distance between any two staggered bolts (L) are presented in Fig. 2. Two types of bolt stagger pattern were studied, namely, patterns P1 and P2 with two- and three-bolt lines (parallel to the loading direction), respectively. Two M12 bolts (Grade 12.9) were used in each bolt line. The bolt diameter (d_0) was 13 mm. The nominal thickness (t) of the main plate was 5 mm, 6 mm and 6 mm for the Q960, Q690 and Q345 specimens, respectively. Q690 steel plates with t = 10 mm were employed to fabricate all the lap plates. The gauge (g) was ranged from 16 mm to 70 mm. The pitch (s) was varied from 10 mm to 42 mm. The end distance (e_1) and the edge distance (e_2) were maintained at 40 mm and 16 mm, respectively. The specimens were designated by a set of letters and numbers. The steel grades Q345, Q690 and Q960 were represented by the letters M1, M2, and M3, respectively.

Take specimen P1G30S15M1 as an example, 'P1' represents Pattern 1 arrangement of the bolt holes, as presented in Fig. 2a, 'G30' means the gauge g = 30 mm, 'S15' means pitch s = 15 mm, and 'M1' means the steel grade Q345. As shown in Table 1, the specimen dimensions in the study satisfy the geometric limits of EN 1993-1-8, except three specimens (i.e., P1G16S22M1, P1G16S22M2 and P1G16S22M3) with L = 27 mm, slightly less than the minimum value of 31 mm. Table 2 summarises the measured dimensions.

To obtain the mechanical property of the steel materials, three plate-type tensile coupons were tested for each steel grade according to ASTM A370-17 [28]. Fig. 3 shows the typical dynamic and static stress-strain curves of the three grades of steel material. Table 3 summarises the average values of the material properties, which were determined by the static stress-strain curves, such as the elastic modulus (E), yield strength (f_y), tensile strength (f_u), ultimate strain (ε_u) and elongation at fracture (Δ) based on a gauge length of 50 mm.

2.2 Test setup and procedures

The test was conducted by a servo-hydraulic testing system (INSTRON 8803). The longitudinal axis of the test specimens was carefully aligned with that of the tension test machine to minimise the effect of any angular distortion of the specimens on the test results. As shown in Fig. 4, a green laser line was projected onto the specimen surface and adjustments were made accordingly to bring the test setup into good alignment both before and after clamping the grips. A quasi-static tensile load was applied to the bottom end of the specimen by the bottom hydraulic grip, and the other end was fixed to the top grip. The applied load level was recorded by the built-in load cell. In addition, the elongation of the specimens was measured by two linear variable differential transformers (LVDTs), as shown in Fig. 4. The bolts were tightened to a snug tight condition by an ordinary spud wrench according to RCSC

2020 [29], in order to minimise the frictional resistance of the specimens.

To minimise major slip due to the bolt-hole clearance, a 10 kN preload was applied to the specimens. Subsequently, the applied load was lowered to 2 kN to ensure that the bolts still bore on the walls of bolt holes. In the elastic stage, the load was applied using a load control. In the inelastic stage, a stroke control was employed with a rate of 0.5 mm/min and 0.3 mm/min for the MS and HSS specimens, respectively. The loading rate was subsequently increased to 1.0 mm/min and 0.5 mm/min at the post-ultimate state, respectively. At each loading step, the load was paused for around 120 seconds in order to obtain the static load values.

2.3 Test results

Fig. 5 shows the typical failure mode of the specimens. All the specimens failed in net section fracture through the first staggered row of bolt holes as predicted by the $s^2/4g$ rule (blue dash line). The fracture path initiated on the main plate at the location where the plate thickness was reduced the most. This observation will be further demonstrated in the following discussion. Table 2 summarises the test results, including the test ultimate load ($P_{u,test}$) and the connection efficiency of the specimens, i.e., the ratio of $P_{u,test}$ to the net section resistance (P_{us}). P_{us} is equal to $A_{net}f_u$, where the staggered net section area A_{net} was determined by the $s^2/4g$ rule. It was found that almost all the staggered bolted connection specimens could achieve the corresponding net section resistance ($A_{net}f_u$). For the Q345 specimens, the connection efficiency ranged from 0.99 to 1.11 with a mean value of 1.05 and a coefficient of variation (CoV) of 3.7%. For the Q690 specimens, the connection efficiency varied from 0.97 to 1.09 (mean value = 1.03, CoV = 4.0%). For Q960 specimens, the corresponding values ranged from 0.97 to 1.06 (mean value = 1.01, CoV = 3.3%).

In general, the typical load-displacement curves of the specimens show similar responses, where the displacement (d) is the average readings of the two LVDTs (d_1 and d_2), as depicted in Fig. 6. Initially, the displacement (d) increased almost linearly with increasing applied load, and a nonlinear load-displacement response was subsequently observed after the material yielded. The MS specimens exhibited a larger deformation than that of the HSS specimens before the attainment of the corresponding ultimate load due to the high ductility of the MS material. The ultimate load of the MS specimens was achieved when the displacement (d) was between 2.5 mm and 4.0 mm. However, the HSS specimens reached the ultimate state quickly after nonlinear load-deflection behaviour was observed, and the corresponding displacement at ultimate was only between 1.0 mm and 2.0 mm, as shown in Fig. 6. This is because of the lower ductility and lower f_u/f_y ratio of the HSS materials which caused the net section fracture of the connection to occur prior to further elongation of the member. Similar test behaviour was also observed for the other specimens. The overall deformation of all specimens will be further analysed in the following discussion of test results.

The strains along the staggered path (black dash line) were measured by two strain gauges (SG#1 and SG#2) mounted on the plate edges and two rosettes (SGR#1 and SGR#2) along the inclined path, as illustrated in Fig. 7. Specimens P1G55S32M1, P1G55S32M2 and P1G55S32M3 with enough clear space for installing the rosettes were selected for examining the strain development along the staggered path. The corresponding load versus strain curves along the loading direction are shown in Fig. 8. In general, yielding occurred in the plate edges initially due to the short length of the plate edge. For specimen P1G55S32M1, the material along the inclined path started to yield when the load was increased to around 70% of the corresponding ultimate load, i.e., $0.7P_{u,test}$, as shown in Fig. 8a. For the HSS specimens, however, yielding of the material along the inclined path did not occur until the load was close to $0.9P_{u,test}$ due to the lower f_u/f_y ratio of HSS material, as shown in Figs. 8b and 8c. Subsequently, the load approached the ultimate level rapidly with a further increase in strain.

2.4 Discussion of test results

In general, for the specimens with the same staggered bolt pattern, the corresponding ultimate load increases with increasing pitch and gauge distance, as summarised in Table 2. However, there is a slight decrease of the test ultimate load among specimens P1G55(S15-S32)M1, P1G55(S15-S32)M2 and P1G55(S15-S32)M3, with a reduction percentage no more than 1%. In addition, the connection efficiency of the specimens decreases with an increase in pitch (*s*) for the specimens with the same gauge (*g*), as shown in Fig. 9. For the specimens with a gauge of 30 mm, i.e., P1G30(S15-S32)M1, P1G30(S15-S32)M2 and P1G30(S15-S32)M3, the connection efficiency decreases from 1.08 to 0.99, 1.04 to 0.98 and 1.01 to 0.97, respectively, with an increase in pitch from 15 mm to 32 mm, as shown in Fig. 9a. For the specimens with a gauge of 40 mm and 55 mm, a similar decline trend was also observed, as illustrated in Figs. 9b and 9c, respectively. This was consistent with the findings by Epstein and Gulia [18], suggesting that the prediction accuracy of the $s^2/4g$ rule was influenced by the pitch and gauge. Fig. 9d shows that specimens P2G30(S10-S22) in pattern P2 always have higher connection efficiencies in contrast to the specimens P1G30(S10-S22) with the same s/g ratio but in pattern P1 irrespective of the steel grade, echoing the finding by Jiang *et al.* [22]. In addition, the connection efficiency is less than 1.0 for the specimen with a large s/g ratio, such as specimens P1G30S32(M1-M3), P1G40S32(M1-M3), etc., as shown in Table 2. It may be attributed to the effect of biaxial stress state across the staggered net section, which may decrease with increasing s/g ratio and may also be influenced by the bolt stagger pattern. To better interpret these test observations, a finite element analysis of the specimens was conducted, and the results will be presented in the following section.

For the specimens with the same geometric configuration, (including the stagger pattern, the gauge, and the pitch), the overall displacements at the ultimate state of the Q345 specimens are much larger than those of Q690 and Q960 specimens, as shown in Figs. 6 and 10a. This observation is expected since the Q345 material possesses much larger ductility than those of the HSS materials, which allows effective stress redistribution to occur along the staggered net section. Thus, the MS specimens were able to sustain further deformation along the loading direction prior to staggered net section fracture, echoing the finding by Wei *et al.* [19]. As shown in Table 2, the ultimate loads of the specimens increased when a higher steel grade was used due to the increase in the material strength. However, the connection efficiency of the specimens with a higher steel grade decreased as shown in the table. For some of the HSS specimens, the connection efficiency even declined to below 1.0, as shown in Table 2 and Fig. 10b. This might be attributed to the lower ductility and lower f_u/f_y ratio of HSS materials, which prohibited an effective stress redistribution to occur along the staggered net section prior to fracture.

The fracture path was examined via the deformation process along the staggered net section. Specimens P1G40S32M1, P1G40S32M2 and P1G40S32M3 were unloaded after each displacement increment, and the lap plates were then removed to examine the deformation of the main plate, as shown in Fig. 11. In Huns *et al.* [30], the steel bolted connection specimen T1A was also tested by a similar loading and unloading scheme and the other specimen T1B with the same geometric configuration was loaded continuously at a displacement rate of 1.0 mm/min. It was found that the test ultimate load of specimen T1A (696.0 kN) was similar to that of specimen T1B (690.8 kN), with a difference of 0.7%. Therefore, it is believed that the loading and unloading scheme used in this study would not significantly influence the test ultimate load of specimens P1G40S32M1, P1G40S32M2 and P1G40S32M3. At each unloading stage, the thickness of the bolt hole edge at eight specific points, namely, A to H was measured using a point micrometre (0~25 mm/0.01 mm). The arrangement of these points is shown in Fig. 7. The detailed deformation process of the main plate is briefly presented as follows.

As shown in Fig. 11, the first unloading stage was carried out when the specimen began to exhibit inelastic behaviour. At this stage, the mill scale on the surface of the main plate started to peel off and slight deformation of the bolt holes was observed on specimen P1G40S32M1, as shown in Fig. 11a. At the 7th unloading stage, obvious plastic deformation occurred at the bolt holes and the plate edges. The ultimate load was achieved between the 9th and 10th unloading stages. Significant necking of the plate edges developed in the following two stages and fracture occurred in the plate edge near point A at the 12th unloading stage, as shown in Fig. 11a. For the HSS specimens, the deformation of the bolt holes became significant when approaching the ultimate state, i.e., near the 6th and 5th unloading stages for specimens P1G40S32M2 and P1G40S32M3, respectively, as shown in Figs. 11b and 11c. For specimen P1G40S32M2, fracture of the two plate edges occurred at the 10th unloading stage, as shown in Fig. 11b. For specimen P1G40S32M3, fracture occurred in the plate edge near point A at the 8th unloading stage. The fracture of the plate edge near point E started at the 9th unloading stage and completed at the 10th unloading stage, as shown in Fig. 11c.

The initial position of the fracture path on the bolt hole edge was identified as the location at which the maximum reduction in plate thickness near the ultimate state occurred. It was observed that the identified positions on the inside edges of BH#1and BH#2 varied with the level of the applied load but always located between points B and C, and points F and G, respectively (i.e., the red curve segments in Fig. 12). This means that the initial locations of the fracture path identified from the test are different from those determined by the line joining the centre of the staggered bolt holes, as shown in Fig. 12. The thickness of the main plate at 10th, 6th and 5th unloading stages was taken as the value at the corresponding ultimate state for specimen P1G40S32M1, P1G40S32M2 and P1G40S32M3, respectively. The measured values of plate thickness at points A and E, and the smallest plate thickness on the inside edge of bolt holes (BH#1 and BH#2) at the ultimate state was decreased by 31%, 23%, 15% and 15%, respectively for specimen P1G40S32M1 from the original thickness (t) of 5.81 mm. For specimen P1G40S32M2 with $t = 5.84$ mm, the corresponding reduction in plate thickness was 14%, 15%, 8% and 9% for these four locations, respectively. For specimen P1G40S32M3 with $t = 4.84$ mm, the reduction was 16%, 13%, 6% and 5%, respectively, as shown in Fig. 12.

For these three specimens, therefore, fracture occurred at the plate edges initially, followed by the fracture of the inclined path between the bolt holes BH#1 and BH#2. The fracture of HSS specimens occurred at the earlier loading stage comparing with that of the MS specimen because of the lower ductility and lower f_u/f_y ratio of the HSS material. Furthermore, the test observations indicated that the actual fracture path of the staggered net section was not exactly consistent with the line joining the corresponding centre of the bolt holes as assumed in the $s^2/4g$ rule. This will be further discussed in the following section of FE analysis.

3. Finite element analysis

3.1 Modelling strategy

The structural behaviour of the specimens was numerically investigated by FE analysis via ABAQUS/Explicit (6.14) [31]. All the components such as the lap plates, the main plates and the bolts were modelled by solid element C3D8R, as shown in Fig. 13. For the bolt and lap plate, the mesh size was maintained at approximately 2.0 mm and 4.0 mm, respectively. A mesh study was conducted to determine the optimal mesh size for the area around the first row of the staggered bolt holes in the main plate which is the location of fracture initiation. The element size of 3.0 mm, 2.0 mm, 1.0 mm and 0.5 mm were used in the mesh convergence study.

Fig. 14 shows that the predicted load-displacement curves of specimen P1G40S32M2 based on mesh sizes (3) and (4) agreed well. To reduce the computation time, mesh size (3), i.e., the element size of 1.0 mm and 2.0 mm around the first and second row of staggered bolt holes, respectively, were used in this study. The boundary conditions were defined as those in the tests, i.e., one end of the specimen was fixed and the other end was loaded in the longitudinal direction (U1) using displacement control, as shown in Fig. 13d. Initial contact between the bolt hole and bolt shank was also set. General contact with "hard" contact was adopted to define the normal direction behaviour of the contact surfaces between the bolt holes and the shanks, and between the main plates and the lap plates, etc. The friction coefficient was specified to be 0.2 for the tangential contact behaviour [32].

Since the test connections were subject to monotonic loading, the plastic material behaviour of all connected components was described by the classical J_2 plasticity with isotropic hardening law [33-35]. Before necking, the true strain and stress was obtained by $\ln(1+\varepsilon_{eng})$ and $\sigma_{eng}(1+\varepsilon_{eng})$, respectively, where σ_{eng} and ε_{eng} are the engineering stress and strain, which were obtained from the tensile coupon tests in this study. For the M12 bolt (Grade 12.9), material properties were adopted from [36], i.e., E = 211 GPa, f_y = 1210 MPa, f_u = 1310 MPa, and ε_u = 3.25%. In the post-necking stage, the true stress-strain relationship cannot be obtained directly based on the engineering stress and strain [37]. Hence, several methods were proposed to determine the post-necking true stress-strain relationship. Bridgman [37] first suggested a linear relation between the post-necking true stress and strain, which requires complicated measurements and could not be applied to a coupon with a rectangular section. Ling [38] proposed a weighted average method based on a power-law curve (lower bound assumption) and a linear relation (upper bound assumption) for the post-necking true stress-strain relationship, which is applicable to the flat tensile bars. However, the lower bound was found to overestimate the post-necking true stress for some metals [39]. Jia and Kuwamura [39] subsequently proposed a modified weighted average method using a linear relation for the lower and upper bound cases. The true post-necking stress-strain relationship can be obtained by a trial-and-error procedure until the numerical results agreed well with the experimental results. The modified weighted average method to determine the true post-necking stress-strain relationship was supported by recent research studies [40-42]. In this study, therefore, the true stress-strain relationship in the post-necking stage was determined based on this approach.

In order to predict the corresponding fracture behaviour, the simplified Johnson-Cook fracture model was employed [43-45].

$$\bar{\varepsilon}_f^{pl} = C_1 + C_2 e^{-C_3 \eta} \tag{3}$$

where η is the stress triaxiality, $\bar{\varepsilon}_f^{pl}$ is the equivalent plastic strain to fracture [44, 46]. To simulate the fracture, the related elements were deleted from the model when the damage index $\int_0^{\bar{\varepsilon}_f^{pl}} (L/\bar{u}_f^{pl})\, d(\bar{\varepsilon}^{pl})$ reached 1.0 [31], where L is the element characteristic length, which is calculated by ABAQUS automatically, $\bar{u}_f^{pl}$ is the effective plastic displacement corresponding to a failure point and was specified to be 0.1, and the evolution in the damage was assumed to be a linear relationship [47]. Due to a lack of material test data, a trial-and-error approach was adopted to calibrate the material parameters C_1, C_2, and C_3 such that a satisfactory agreement between the FE analysis results and the test results in the descending branch of the load versus displacement response of the specimens was obtained [48, 49]. Finally, the values of the calibrated parameters are $C_1 = 0.08$ and $C_2 = 2.0$ for each steel grade, $C_3 = 3.0$ for Q345 material, $C_3 = 2.6$ for Q690 material, and $C_3 = 3.3$ for Q960 material.

3.2 **Finite element analysis result**

Table 2 summarises the ratio of the test ultimate loads ($P_{\mathrm{u,test}}$) to those predicted by the FE analysis ($P_{\mathrm{u,FEM}}$), i.e., $P_{\mathrm{u,test}}/P_{\mathrm{u,FEM}}$. For the Q345 specimens, the corresponding ratio varied from 0.97 to 1.01 (mean value = 0.99, CoV = 1.4%). For the Q690 specimens, the $P_{\mathrm{u,test}}/P_{\mathrm{u,FEM}}$ ratio varied from 0.94 to 1.03 (mean value = 1.00, CoV = 1.9%). For the Q960 specimens, the ratio varied from 0.96 to 1.01 (mean value = 0.99, CoV = 1.5%).

As presented in Fig. 5, the staggered net section fracture of the specimens predicted by the FE analysis agreed well with the failure mode of the specimens observed in the tests. Fig. 6 shows that the FE load-displacement curves compared well with those from the test results. The FE load versus strain behaviour along the loading direction was in reasonable agreement with those obtained from the tests, as shown in Fig. 8. It should be noted that the readings of the two strain gauges (SG#1 and SG#2) on specimen P1G55S32M1 were not similar, which was different from the observations in specimens P1G55S32M2 and P1G55S32M3. This was because the actual location of strain gauge SG#2 on specimen P1G55S32M1 was not right at the middle of the plate edge but instead near the plate edge, resulting in the reading of SG#2 smaller than that of SG#1 at the same load level. In Fig. 8, the predicted strain was extracted at the locations as those in the test. In addition, Fig. 11 shows the predicted deformation of the main plate and the corresponding equivalent plastic strain (PEEQ) contours at various unloading stages. The deformation behaviour of the main plate, especially for the post-ultimate stage such as necking of the plate edges, the sequence of plate fracture occurrence and the position of fracture, was well captured by the FE analysis. Furthermore, the smallest plate thickness on the inside edges of the bolt holes at the ultimate state predicted by the FE analysis (t_{FE}) was extracted from specimens P1G40S32M1, P1G40S32M2 and P1G40S32M3, as shown in Figs. 15a to 15c. These predicted values are in good agreement with the measured values of thickness from the tests (t_{test}) with a maximum difference less than 3.0%.

The above has demonstrated that the FE model was able to predict well the structural behaviour and the ultimate loads of the specimens. Based on the validated FE model, the effects of *s/g* ratio on the fracture path and on the biaxial stress state along the staggered net section were further investigated. As shown in Figs. 15a to 15c, the initial positions of the fracture path on the bolt hole inside edges, which were identified by the smallest predicted plate thickness at the ultimate state, were similar for the three specimens with the same *s/g* ratio of 0.8. However, for specimens P1G30S15M2, P1G30S22M2 and P1G30S32M2 (Figs. 15d to 15f), the corresponding fracture positions varied with the *s/g* ratio ranging from 0.5 to 1.1. The initial position of the fracture path on the inside edge of the bottom bolt hole moved upwards along the hole edge slightly with increasing *s/g* ratio. Hence, it may be concluded that the *s/g* ratio could affect the fracture path position and the corresponding length of the fracture path. Fig. 16 shows a comparison of the length between the inclined path predicted by the FE analysis (L_{FE}) and the commonly adopted theoretical fracture path (L_{d}), which is defined as $\sqrt{s^2+g^2}-d_0$. It can be found that L_{FE} was generally slightly larger than L_{d} with a maximum difference of 6.6%. Therefore, the length of the actual fracture path between the staggered bolt holes was generally underestimated by that of the theoretical fracture path, which was assumed to be the line joining the corresponding centre of the staggered bolt holes.

The stress vector plots at the loading stage of $0.9P_{\mathrm{u,FEM}}$ for specimens P1G30S32M2, P1G30S15M2 and P2G30S15M2 with different *s/g* ratios and different stagger patterns are shown in Figs. 17a to 17c. As shown in the figures, the biaxial stress state exists in the areas near the bolt holes, and between the staggered bolt holes. The enlarged views of the stress plots in areas R_1~R_5 are shown in Figs. 17d to 17f. Obvious biaxial tensile stress state in the area adjacent to the outside edge of the bolt holes (i.e., areas R_1 and R_2) is observed in the three specimens. Because of the biaxial stress effect, higher axial stress (S_{11} in Fig. 17) is required in order for the plate material to reach the corresponding material tensile strength [10, 11]. This finding is consistent with that in the previous study on connections without staggered bolts [6]. However, for specimen P1G30S15M2 with a smaller value of s/g ratio (s/g = 0.5), a small biaxial tensile stress state was observed adjacent to the inside edge of the bolt holes (i.e., areas R_3 and R_5), while in the middle area (i.e., area R_4), there was no appreciable biaxial stress state, as shown in Fig. 17e. For specimen P1G30S32M2 with an s/g ratio of 1.1, the stress state in areas R_3~R_5 became biaxial tensile-compressive stress, as shown in Fig. 17d, which reduced the applied axial stress required to reach the material strength in the areas [11]. Therefore, the connection efficiency was smaller than 1.0 for the connections with a relatively larger value of s/g ratio, as shown in Table 2. Besides, this helps explain that the connection efficiency decreases with increasing pitch (s), as shown in Figs. 9a to 9c. As shown in Table 2, specimens P2G30S15M2 and P1G30S15M2 have the same s/g ratio but different stagger patterns. Figs. 17c and 17f show that the biaxial tensile stress was more significant for specimen P2G30S15M2 than that of specimen P1G30S15M2. This is possibly due to the symmetrical arrangement of the three bolt holes along the staggered net section for pattern P2. Hence, the strength of the net section was consequently increased by the biaxial tensile stress effect. This finding helps explain the observation that the connection efficiencies of P2 series connections are higher than those of the P1 series with the same s/g ratio, as shown in Fig. 9d.

4. Reliability analysis

As specified in EN 1993-1-12 [2], the net section resistance of HSS up to S700 could be determined by Eq. (1). In a previous study, the authors have suggested that for HSS bolted connections without a staggered pattern, the net section resistance could be predicted conservatively by this equation with a partial factor γ_{M12} = 1.25 [6]. In this study, however, the net section resistance $A_{net}f_u$, where A_{net} was determined by the $s^2/4g$ rule, was over-estimated for the HSS specimens with a relatively large *s*/*g* ratio. Therefore, a reliability analysis was conducted based on 48 test data, including 33 from this study and 15 from Jiang *et al.* [22] to evaluate the applicability of Eq. (1) to staggered bolted connections made using HSS up to Q960.

In Eurocode, the target level of reliability was obtained by partial factor design. In this section, the evaluation of the partial factor was conducted according to the standard procedure as specified in EN 1990 [50]. The partial factor γ_{M} is defined as the ratio of the characteristic to the designed resistance to account for uncertainties of the model and the material properties, as well as the variations in dimensions [50], expressed as

$$\gamma_M = \frac{r_k}{r_d} \tag{4}$$

$$r_k = b g_{rt}(\underline{X}_m) \exp(-k_\infty \alpha_{rt} Q_{rt} - k_n \alpha_\delta Q_\delta - 0.5Q^2) \tag{5}$$

$$r_d = b g_{rt}(\underline{X}_m) \exp\left(-k_{d,\infty} \alpha_{rt} Q_{rt} - k_{d,n} \alpha_\delta Q_\delta - 0.5Q^2\right) \tag{6}$$

where $g_{rt}(\underline{X}_{\mathrm{m}})$ is the design model, i.e., $A_{\mathrm{net}}f_{\mathrm{u}}$ in this study, the corresponding value was determined based on the nominal dimensions and measured material properties. The average value of correction factor b is presented as $\sum r_{\mathrm{e}} r_{\mathrm{t}} / \sum {r_{\mathrm{t}}}^2$, where r_{e} and r_{t} are the resistance obtained from experiment and theoretical calculation, respectively. The values of characteristic and design fractile factors, i.e., k_{n} and $k_{\mathrm{d,n}}$, were determined based on the test number *n* [51, 52]. For infinite *n*, $k_\infty = 1.64$ and $k_{\mathrm{d},\infty} = 3.04$ [50]. Parameters, including Q_{rt}, Q_δ and Q were obtained by the expressions of $\sqrt{\ln(\sum_{i=1}^{j} {V_{\mathrm{Xi}}}^2 + 1)}$, $\sqrt{\ln({V_\delta}^2 + 1)}$, and $\sqrt{\ln({V_{\mathrm{r}}}^2 + 1)}$, respectively, where coefficients of variation $V_{\mathrm{r}} = \sqrt{{V_\delta}^2 + \sum_{i=1}^{j} {V_{\mathrm{Xi}}}^2}$, *j* is the number of the variation (V_{Xi}) in the design model. The CoV value of the tensile strength of HSS material was taken as 0.055 [53]. The CoV of the plate width, hole spacing, and hole diameter were all considered to be 0.005. For the plate thickness, the CoV was taken as 0.05 [54, 55]. Parameters α_{rt} and α_{δ} are equal to Q_{rt}/Q and Q_{δ}/Q, respectively.

It is worth noting that the partial factor γ_{M} should be modified since the value of the characteristic resistance is different from the corresponding nominal resistance. Factor k_{c} which is the ratio of the nominal resistance (r_{n}) to the characteristic resistance, i.e., $k_{\mathrm{c}} = r_{\mathrm{n}}/r_{\mathrm{k}}$ was introduced. In the current research, r_{n} was determined by the characteristic value of the measured material property and the nominal dimensions, expressed as

$$r_n = g_{rt}(\underline{X}_n) = g_{rt}(\underline{X}_m)exp(-2.0V_r - 0.5{V_r}^2) \tag{7}$$

where the value of V_{r} was equal to the maximum coefficient of variation based on the previous tests. Finally, the corrected partial factor ${\gamma_{\mathrm{M}}}^*$ is obtained by

$${\gamma_M}^* = k_c\gamma_M = \frac{r_n}{r_k}\cdot\frac{r_k}{r_d} = \frac{r_n}{r_d} \tag{8}$$

Based on the above procedure, the HSS connections test data from the current study was then evaluated statistically. Table 4 summarises the results of the statistical analysis. It can be seen that the corrected partial factor ${\gamma_{\mathrm{M}}}^*$ is equal to 1.126 for the design model $A_{\mathrm{net}}f_{\mathrm{u}}$. For another design model with a factor of 0.9, i.e., $0.9A_{\mathrm{net}}f_{\mathrm{u}}$, the value of ${\gamma_{\mathrm{M}}}^*$ was reduced to 1.014. It indicates that the net section resistance of HSS staggered bolted connections can also be predicted conservatively by the current design equation in EN 1993-1-12.

5. Summary and conclusions

This study investigated the net section resistance of HSS staggered bolted connections experimentally and numerically. 48 bolted connection specimens were tested including 15 mild steel and 33 high strength steel specimens. All the specimens failed in net section fracture through the staggered path. Based on the test results, it was found that almost all the connection specimens could reach the corresponding net section resistance ($A_{net}f_u$). The average connection efficiency was 1.05, 1.03 and 1.01 for the Q345, Q690 and Q960 connection specimens, respectively. In addition, the HSS specimens exhibited much lower deformation capability compared with that of the MS specimens because of the lower ductility of HSS material.

The structural behaviour of the specimens was further studied by finite element (FE) analysis. The FE analysis results indicated that the stress redistribution along the staggered net section for the HSS specimens was not significantly influenced by the lower ductility and lower f_u/f_y ratio of HSS materials when compared with those of MS materials. Based on the validated FE model, the length of the predicted failure path was also compared with the corresponding theoretical value according to the $s^2/4g$ rule. It was found that the length of the fracture path of the staggered net section was underestimated slightly by the $s^2/4g$ rule.

The HSS connection specimens with a small s/g ratio were able to achieve the corresponding net section strength ($A_{net}f_u$) because of the effective stress redistribution along the staggered net section combined with the beneficial effect of biaxial stress state. However, for the specimens with a large s/g ratio, the stress state across the staggered segment was changed to biaxial tensile-compressive stresses, which decreased the net section strength of the specimens. Thus, the corresponding net section resistance was slightly overestimated by $A_{net}f_u$.

Finally, the results of the 33 HSS specimens from the current study was statistically analysed to re-evaluate the partial factor adopted in the current design formula. Based on the analysis results, the corrected partial factor γ_M^* was equal to 1.126 for the design model $A_{net}f_u$, which was further decreased to 1.014 for the design model with a factor of 0.9, i.e., $0.9A_{net}f_u$. It may be concluded that for HSS staggered bolted connections, the corresponding net section resistance predicted by the current design equation in EN 1993-1-12 was conservative, where A_{net} can be determined by the $s^2/4g$ rule and the partial factor is equal to 1.25. It should be noted that the conclusions were based on the limited test data provided in this study. Special caution of using the research findings should be taken if different dimensions of the connections or different bolt pattern arrangements are used.

Acknowledgements

The work described in this paper is fully supported by a grant from the Chinese National Engineering Research Centre (CNERC) for Steel Construction (Hong Kong Branch) at The Hong Kong Polytechnic University (Project No. 1-BBYQ). The technical assistance during the experimental investigation provided by Mr C.F. Wong and Mr M.C. Ng is gratefully acknowledged.

References

[1] Günther H-P. Use and application of high-performance steels for steel structures. Switzerland: IABSE-AIPC-IVBH; 2005.

[2] CEN. Eurocode 3: Design of steel structures-Part 1-12: Additional rules for the extension of EN 1993 up to steel grades S700. BS EN 1993-1-12. London: European Committee for Standardization (CEN); 2007.

[3] Jiang K, Zhao O, Tan KH. Experimental and numerical study of S700 high strength steel double shear bolted connections in tension. Eng Struct. 2020;225:111175. https://doi.org/10.1016/j.engstruct.2020.111175.

[4] Može P. Statistical evaluation of bearing resistance and related strength functions for bolted connections. J Constr Steel Res. 2020;171:106128. https://doi.org/10.1016/j.jcsr.2020.106128.

[5] Feldmann M, Schillo N, Schaffrath S, Virdi K. Rules on high strength steel (RUOSTE). EUR 28111EN. Luxembourg: European Commission; 2016. https://doi.org/10.2777/908095.

[6] Lin X-M, Yam MCH, Chung K-F, Lam ACC. A study of net-section resistance of high strength steel bolted connections. Thin-Walled Struct. 2021;159:107284.

https://doi.org/10.1016/j.tws.2020.107284.

[7] Schutz J, Frederick W, Newmark N. The efficiency of riveted structural joints. University of Illinois Engineering Experiment Station, University of Illinois at Urbana-Champaign; 1952.

[8] Munse WH, Chesson E. Riveted and bolted joints: net section design. J Struct Div-ASCE. 1963;89:107-26.

[9] Fisher JW. On the behavior of fasteners and plates with holes. Fritz Engineering Laboratory, Department of Civil Engineering, Lehigh University; 1964.

[10] Nádai A. Theory of flow and fracture of solids, Vol. 1. New York: McGraw-Hill; 1950.

[11] Timoshenko S. Strength of materials: Part I. Elementary theory and problems. Second ed. England: D. Van Nostrand Co., Inc; 1948.

[12] Kulak GL, Fisher JW, Struik JH. Guide to design criteria for bolted and riveted joints, Second Edition. United States of America: American Institute of Steel Construction, Inc; 1987.

[13] Cochrane VH. Rules for rivet hole deductions in tension members. Engineering News-Record. 1922;89:847-8.

[14] CEN. Eurocode 3: Design of steel structures-Part 1-1: General rules and rules for buildings. BS EN 1993-1-1. London: European Committee for Standardization (CEN); 2005.

[15] CSA. Design of steel structures. CSA S16-14. Toronto, Canada: Canadian Standard Association (CSA); 2014.

[16] AISC. Specification for structural steel buildings. ANSI/AISC 360-16. Chicago, America: American Institute of Steel Construction (AISC); 2016.

[17] AS. Steel structures. AS 4100-1998 (R2016). (Incorporating Amendment No1). Sydney, Australia: Standards Australia (AS); 2016.

[18] Epstein H, Gulia F. Finite element studies of bolt stagger effects in tension members. Computers & structures. 1993;48:1153-6.

[19] Wei F, Fang C, Yam MC, Zhang Y. Fracture behaviour and design of steel tensile connections with staggered bolt arrangements. Int J Steel Struct. 2015;15:863-79.

[20] Teh LH, Clements DD. Tension capacity of staggered bolted connections in cold-reduced steel sheets. J Struct Eng. 2011;138:769-76.

[21] Cho Y, Teh LH, Young B, Ahmed A. Net section tension strength of bolted connections in ultra-high strength sheet steel during and after fire. J Constr Steel Res. 2020;172:106237. https://doi.org/10.1016/j.jcsr.2020.106237.

[22] Jiang K, Tan KH, Zhao O. Net section fracture of S700 high strength steel staggered bolted connections. Thin-Walled Struct. 2021;164:107904. https://doi.org/10.1016/j.tws.2021.107904.

[23] Fukumoto Y. New constructional steels and structural stability. Eng Struct. 1996;18:786-91. https://doi.org/10.1016/0141-0296(96)00008-9.

[24] Ho HC, Chung KF, Liu X, Xiao M, Nethercot DA. Modelling tensile tests on high strength S690 steel materials undergoing large deformations. Eng Struct. 2019;192:305-22. https://doi.org/10.1016/j.engstruct.2019.04.057.

[25] Lin XM, Yam MCH, Chung KF, Lam ACC. Net section capacity of high strength steel bolted connections with or without staggered bolts. The 10th International Symposium on Steel Structures (ISSS-2019). Jeju, Korea2019.

[26] CNS. High strength structural steel plates in the quenched and tempered condition. [In Chinese]. GB/T 16270-2009. Beijing, China: Chinese National Standard (CNS), Standards Press of China; 2009.

[27] CNS. Steel plate for building structures. [In Chinese]. GB/T 19879-2015. Beijing, China: Chinese National Standard (CNS), Standards Press of China; 2015.

[28] ASTM. Standard test methods and definitions for mechanical testing of steel products. A370-17. West Conshohocken, United States: ASTM International; 2017.

[29] RCSC. Specification for structural joints using high-strength bolts. Chicago, America: Research Council on Structural Connections (RCSC); 2020.

[30] Huns BBS, Grondin GY, Driver RG. Block shear behaviour of bolted gusset plates. Structural Engineering Report No 248. Edmonton, Alberta, Canada: University of Alberta; 2002.

[31] ABAQUS. ABAQUS analysis user's manual (Version 6.14)2014.

[32] CEN. Eurocode 3: Design of steel structures-Part 1-8: Design of joints. BS EN 1993-1-8. London: European Committee for Standardization (CEN); 2005.

[33] Salih EL, Gardner L, Nethercot DA. Numerical investigation of net section failure in stainless steel bolted connections. J Constr Steel Res. 2010;66:1455-66. https://doi.org/10.1016/j.jcsr.2010.05.012.

[34] Može P, Beg D. A complete study of bearing stress in single bolt connections. J Constr Steel Res. 2014;95:126-40. 10.1016/j.jcsr.2013.12.002.

[35] Lyu Y-F, Wang Y-B, Li G-Q, Jiang J. Numerical analysis on the ultimate bearing resistance of single-bolt connection with high strength steels. J Constr Steel Res. 2019;153:118-29. https://doi.org/10.1016/j.jcsr.2018.10.006.

[36] Pang X-P, Hu Y, Tang S-L, Xiang Z, Wu G, Xu T et al. Physical properties of high-strength bolt materials at elevated temperatures. Results in Physics. 2019;13:102156. https://doi.org/10.1016/j.rinp.2019.102156.

[37] Bridgman PW. Studies in large plastic flow and fracture: McGraw-Hill New York; 1952.

[38] Ling Y. Uniaxial true stress-strain after necking. AMP Journal of Technology. 1996;5:37-48.

[39] Jia L-J, Kuwamura H. Ductile fracture simulation of structural steels under monotonic tension. J Struct Eng. 2014;140:04013115. https://doi.org/10.1061/(ASCE)ST.1943-541X.0000944.

[40] Hu F, Shi G, Shi Y. Constitutive model for full-range elasto-plastic behavior of structural steels with yield plateau: Calibration and validation. Eng Struct. 2016;118:210-27. https://doi.org/10.1016/j.engstruct.2016.03.060.

[41] Shi G, Chen Y. Investigation of ductile fracture behavior of lap-welded joints with 460 MPa steel. Adv Struct Eng. 2017;21:1376-87. 10.1177/1369433217746342.

[42] Yam MCH, Ke K, Jiang B, Lam ACC. Net section resistance of bolted S690 steel angles subjected to tension. Thin-Walled Struct. 2020;151:106722. https://doi.org/10.1016/j.tws.2020.106722.

[43] Bai Y. Effect of loading history on necking and fracture. PhD Massachusetts Institute of Technology, Cambridge, USA. 2007.

[44] Johnson GR, Cook WH. Fracture characteristics of three metals subjected to various strains, strain rates, temperatures and pressures. Eng Fract Mech. 1985;21:31-48. https://doi.org/10.1016/0013-7944(85)90052-9.

[45] Wierzbicki T, Bao Y, Lee Y-W, Bai Y. Calibration and evaluation of seven fracture models. Int J Mech Sci. 2005;47:719-43. https://doi.org/10.1016/j.ijmecsci.2005.03.003.

[46] Rice JR, Tracey DM. On the ductile enlargement of voids in triaxial stress fields∗. J Mech Phys Solids. 1969;17:201-17. https://doi.org/10.1016/0022-5096(69)90033-7.

[47] Adewole KK, Teh LH. Predicting steel tensile responses and fracture using the phenomenological ductile shear fracture model. J Mater Civ Eng. 2017;29:06017019. https://doi.org/10.1061/(ASCE)MT.1943-5533.0002094.

[48] Farahani HK, Ketabchi M, Zangeneh S. Determination of Johnson–Cook plasticity model parameters for Inconel718. J Mater Eng Perform. 2017;26:5284-93. https://doi.org/10.1007/s11665-017-2990-2.

[49] Corona E, Orient GE. An evaluation of the Johnson-Cook model to simulate puncture of 7075 aluminum plates. Sandia National Lab.(SNL-NM), Albuquerque, NM (United States); 2014. https://doi.org/10.2172/1204105.

[50] CEN. Eurocode–Basis of structural design. BS EN 1990: 2002+ A1: 2005. London: European Committee for Standardization (CEN); 2005.

[51] Bond A, Harris A. Decoding Eurocode 7. London: Taylor and Francis; 2008.

[52] Byfield M, Nethercot D. Safety variations in steel designed using Eurocode 3. JCSS Workshop on Reliability Based Code Calibration: Zurich: ETH Zurich; 2002.

[53] Wang J, Afshan S, Gkantou M, Theofanous M, Baniotopoulos C, Gardner L. Flexural behaviour of hot-finished high strength steel square and rectangular hollow sections. J Constr Steel Res. 2016;121:97-109. https://doi.org/10.1016/j.jcsr.2016.01.017.

[54] Snijder HH, Ungermann D, Star JWB, Sedlacek G, Bijlaard FSK, Hernmert-Halswick A. Evaluation of test results on bolted connctions in order to obtain strength functions and suitable model factor. Part A: Results, Background documentation to Eurocode 3. TNO, Brussels: Commission of the European Communities; 1988.

[55] Johansson B, Maquoi R, Sedlacek G. New design rules for plated structures in Eurocode 3. J Constr Steel Res. 2001;57:279-311. https://doi.org/10.1016/S0143-974X(00)00020-1.

Table 1 Comparison between specimen dimensions and geometric limits of EN 1993-1-8

Geometric parameters	Design values	Geometric limits of EN 1993-1-8	Geometric limits in mm (t = 5 mm, d_0 = 13 mm)
e_1	40	$1.2d_0 \leq e_1 \leq 4t + 40$ mm	$16 \leq e_1 \leq 60$
e_2	16	$1.2d_0 \leq e_2 \leq 4t + 40$ mm	$16 \leq e_2 \leq 60$
g	16-70	$1.2d_0 \leq g \leq$ min (14t and 200 mm)	$16 \leq g \leq 70$
s	10-42	-	-
L	27, 31-82	$L \geq 2.4d_0$	$L \geq 31$

Note: the design value of L is obtained by $L = \sqrt{s^2 + g^2}$

Table 2 Measured dimensions of specimens, test results and FE predictions

No.	Specimen	Measured dimensions (mm)						$P_{u,test}$ (kN)	$P_{u,test}$ $/P_{us}$	$P_{u,test}$ $/P_{u,FEM}$
		W	t	d_0	s	g	s/g			
1	P1G30S10M1	62.8	5.7	13.1	10.2	31.3	0.3	129.2	1.06	1.00
2	P1G30S15M1	63.2	5.8	13.1	14.9	30.5	0.5	138.7	1.08	1.01
3	P1G30S22M1	62.3	5.8	13.1	22.2	31.0	0.7	140.9	1.06	1.01
4	P1G30S32M1	62.7	5.8	13.1	32.4	30.2	1.1	147.4	0.99	0.99
5	P1G40S15M1	72.9	5.8	13.1	15.0	40.8	0.4	168.8	1.07	0.98
6	P1G40S22M1	72.7	5.8	13.1	21.7	40.0	0.5	168.9	1.04	0.98
7	P1G40S32M1	72.8	5.8	13.1	31.8	40.7	0.8	172.4	0.99	0.99
8	P1G55S15M1	88.1	5.8	13.1	15.0	54.7	0.3	219.3	1.06	0.97
9	P1G55S22M1	87.9	5.8	13.1	22.3	55.5	0.4	217.5	1.04	0.97
10	P1G55S32M1	87.7	5.8	13.1	31.8	55.6	0.6	216.9	1.00	0.99
11	P1G16S22M1	48.4	5.8	13.1	22.3	16.3	1.4	108.5	1.11	1.00
12	P1G16S27M1	48.8	5.8	13.1	27.0	16.2	1.7	112.1	1.01	0.97
13	P2G30S10M1	92.7	5.8	13.1	10.0	29.7	0.3	199.2	1.10	0.98
14	P2G30S15M1	92.8	5.8	13.1	15.1	30.1	0.5	205.0	1.10	1.00
15	P2G30S22M1	92.7	5.8	13.1	22.1	30.2	0.7	215.0	1.07	1.00
								Mean	1.05	0.99
								CoV	3.7%	1.4%
16	P1G30S10M2	62.8	5.8	13.1	9.6	30.4	0.3	180.1	1.05	1.00
17	P1G30S15M2	62.6	5.8	13.1	15.2	30.3	0.5	184.1	1.04	1.01
18	P1G30S22M2	62.7	5.8	13.1	22.0	30.8	0.7	186.7	1.00	1.01
19	P1G30S32M2	62.8	5.9	13.1	32.0	30.6	1.1	203.0	0.98	0.99
20	P1G40S15M2	72.7	5.9	13.1	14.9	40.5	0.4	230.8	1.04	1.01
21	P1G40S22M2	72.6	5.8	13.1	22.2	39.8	0.6	230.6	1.01	1.01
22	P1G40S32M2	72.8	5.8	13.1	31.8	39.9	0.8	236.8	0.97	1.00
23	P1G55S15M2	87.9	5.8	13.1	15.3	55.3	0.3	305.0	1.06	0.99
24	P1G55S22M2	87.9	5.8	13.1	21.9	55.5	0.4	303.2	1.03	0.99
25	P1G55S32M2	87.4	5.8	13.1	31.9	54.7	0.6	301.6	0.99	1.01
26	P1G16S22M2	48.9	5.8	13.1	21.9	16.8	1.3	149.9	1.09	1.03
27	P1G16S27M2	48.3	5.8	13.0	26.9	16.3	1.7	150.3	0.98	0.94
28	P2G30S10M2	92.6	5.9	13.1	10.2	30.0	0.3	275.5	1.08	0.99
29	P2G30S15M2	92.5	5.8	13.1	14.9	29.9	0.5	286.6	1.09	1.00
30	P2G30S22M2	92.7	5.8	13.1	21.7	30.1	0.7	301.2	1.07	1.01
								Mean	1.03	1.00
								CoV	4.0%	1.9%
31	P1G30S10M3	62.3	4.9	13.1	10.4	30.3	0.3	189.6	1.02	0.98
32	P1G30S15M3	62.8	4.9	13.1	15.2	29.3	0.5	195.2	1.01	0.99
33	P1G30S22M3	62.7	4.9	13.1	22.0	29.9	0.7	201.4	0.98	0.97
34	P1G30S32M3	62.7	4.9	13.1	31.9	30.2	1.1	218.1	0.97	1.00
35	P1G40S15M3	72.3	4.9	13.1	14.9	40.1	0.4	246.5	1.04	1.00

36	P1G40S22M3	72.7	4.9	13.1	21.8	40.4	0.5	248.8	1.00	1.00
37	P1G40S32M3	72.6	4.9	13.1	32.1	39.2	0.8	257.4	0.97	1.01
38	P1G55S15M3	87.4	4.8	13.1	15.0	54.8	0.3	326.5	1.05	0.99
39	P1G55S22M3	87.4	4.8	13.1	21.9	54.5	0.4	323.5	1.02	1.00
40	P1G55S32M3	87.7	4.9	13.1	31.8	54.9	0.6	322.2	0.97	0.99
41	P1G16S22M3	48.7	4.9	13.1	22.0	16.8	1.3	155.9	1.04	0.99
42	P1G16S27M3	48.3	4.9	13.1	26.9	16.3	1.6	161.4	0.97	0.96
43	P1G70S22M3	102.6	4.8	13.1	22.0	69.9	0.3	392.5	1.01	0.96
44	P1G70S32M3	102.4	4.8	13.1	32.0	69.9	0.5	393.7	0.98	0.97
45	P1G70S42M3	102.5	4.9	13.1	42.1	70.0	0.6	401.5	0.97	0.99
46	P2G30S10M3	92.6	4.9	13.1	10.4	30.7	0.3	288.1	1.04	0.96
47	P2G30S15M3	93.0	4.8	13.1	15.1	30.5	0.5	305.2	1.06	0.99
48	P2G30S22M3	93.1	4.8	13.1	22.1	29.9	0.7	323.3	1.04	0.99
								Mean	1.01	0.99
								CoV	3.3%	1.5%

Table 3 Mean value of the measured material properties

Material	Elastic modulus, E (GPa)	Static yield strength, f_y (MPa)	Static tensile strength, f_u (MPa)	Ultimate strain, ε_u (%)	Elongation at fracture, Δ (%)	f_u/f_y
Q345 (t = 6 mm)	210	474	566	13.87	27.44	1.19
Q690 (t = 6 mm)	205	740*	789	6.17	16.78	1.07
Q690 (t = 10 mm)	203	738*	789	6.42	20.15	1.07
Q960 (t = 5 mm)	205	968*	1034	6.25	14.08	1.07

*Note: * - 0.2% proof stress*

Table 4 Results of statistical analyses of design net section resistance

Design model	No. of tests	k_n	k_d	b	V_δ	V_r	k_c	γ_M	γ_M^*
$A_{net}f_u$	48	1.70	3.31	1.039	0.041	0.085	0.995	1.132	1.126
$0.9A_{net}f_u$	48	1.70	3.31	1.154	0.041	0.085	0.896	1.132	1.014

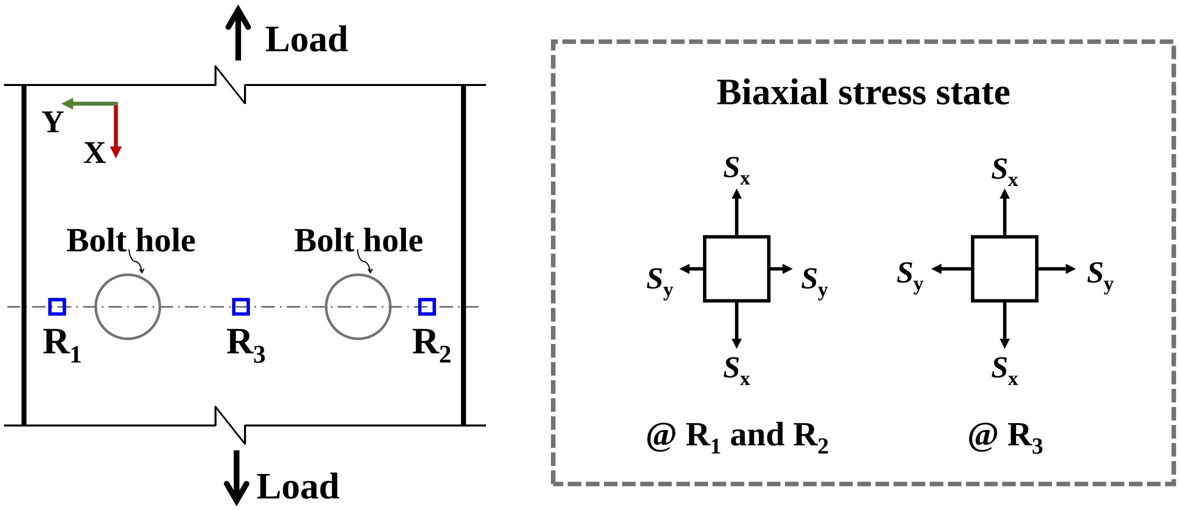

Fig. 1 Biaxial stress state on a perforated plate without a staggered pattern

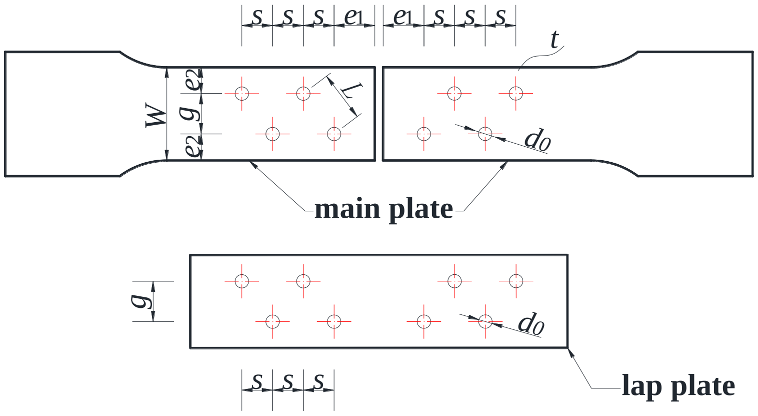

(a) Pattern 1 (P1)

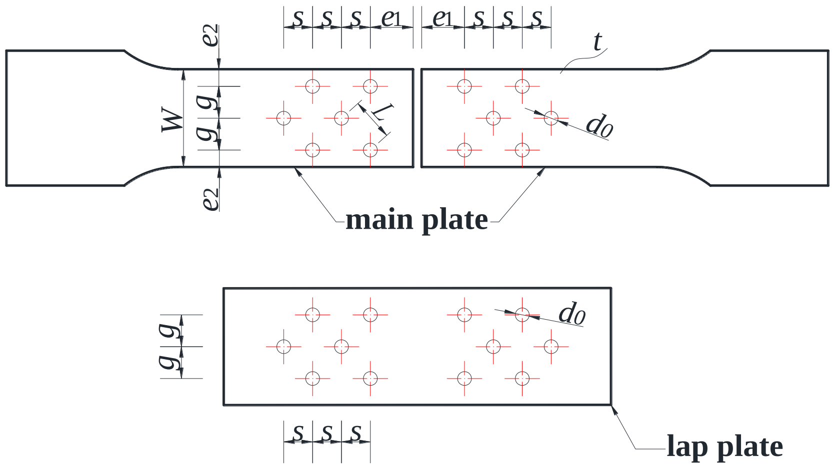

(b) Pattern 2 (P2)

Fig. 2 Geometric configurations of test specimens

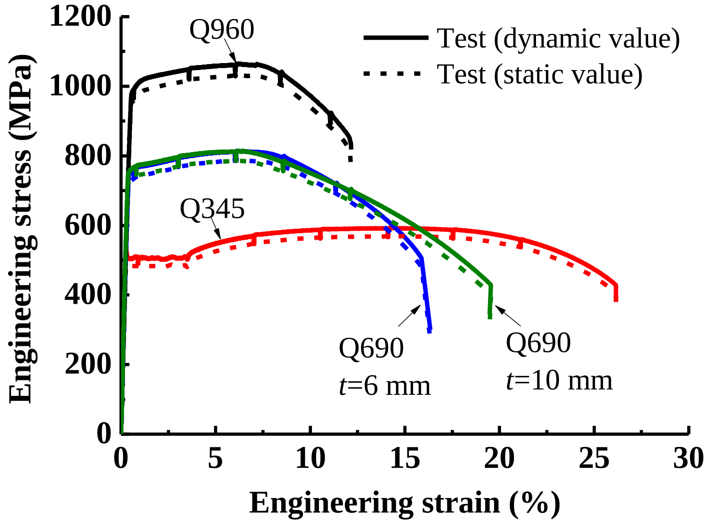

Fig. 3 Typical stress-strain curves of steel materials

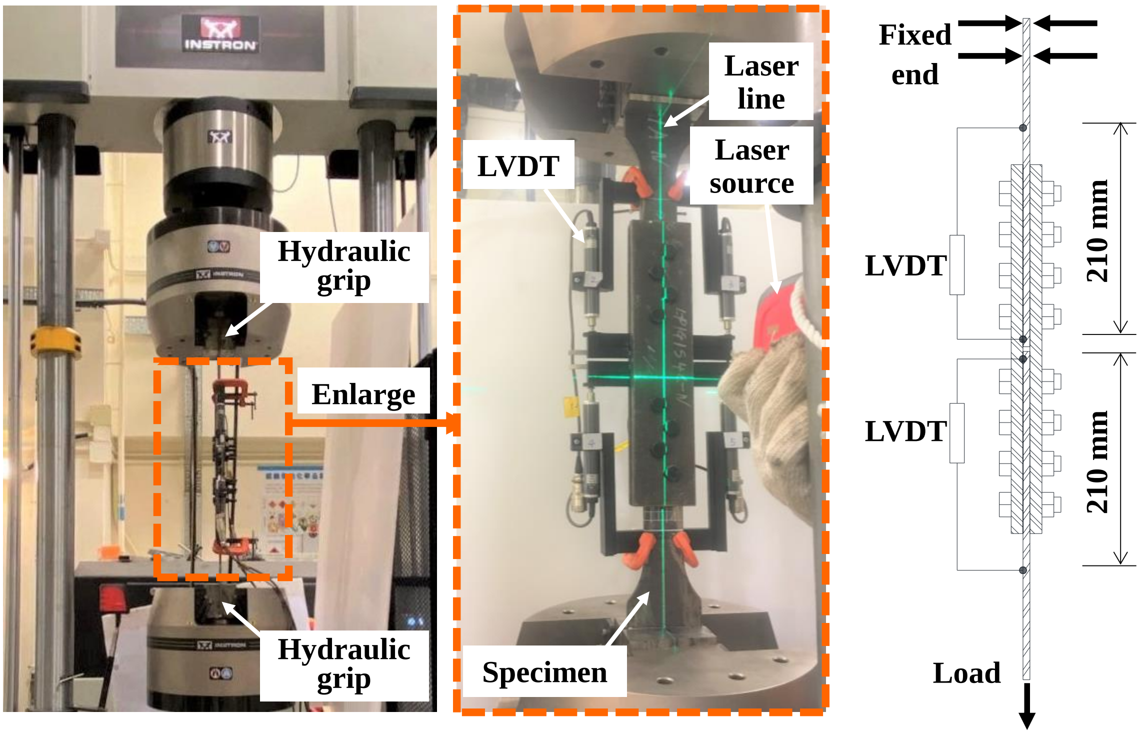

Fig. 4 Test setup

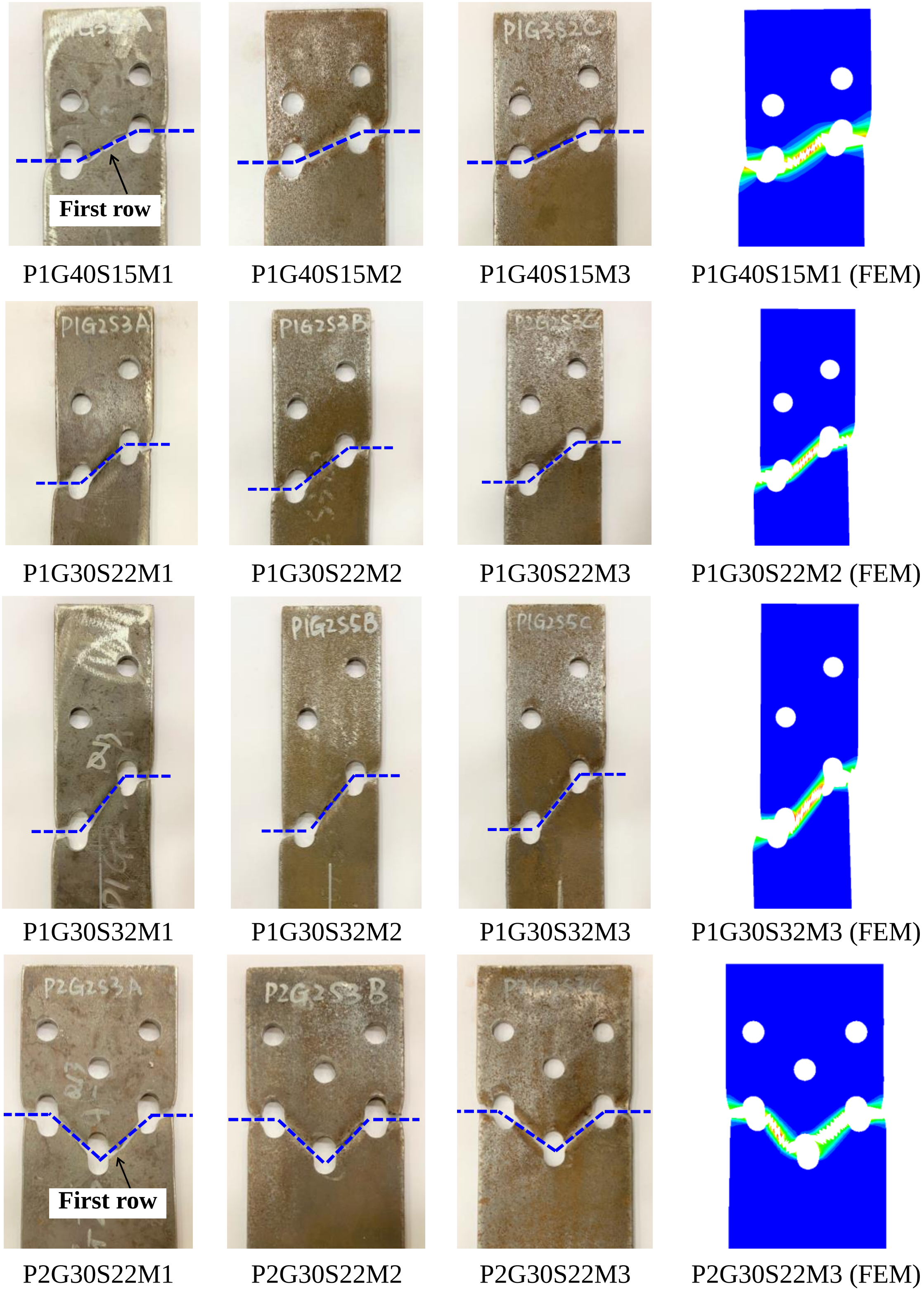

P1G40S15M1 P1G40S15M2 P1G40S15M3 P1G40S15M1 (FEM)

P1G30S22M1 P1G30S22M2 P1G30S22M3 P1G30S22M2 (FEM)

P1G30S32M1 P1G30S32M2 P1G30S32M3 P1G30S32M3 (FEM)

P2G30S22M1 P2G30S22M2 P2G30S22M3 P2G30S22M3 (FEM)

Fig. 5 Typical failure mode of the specimens

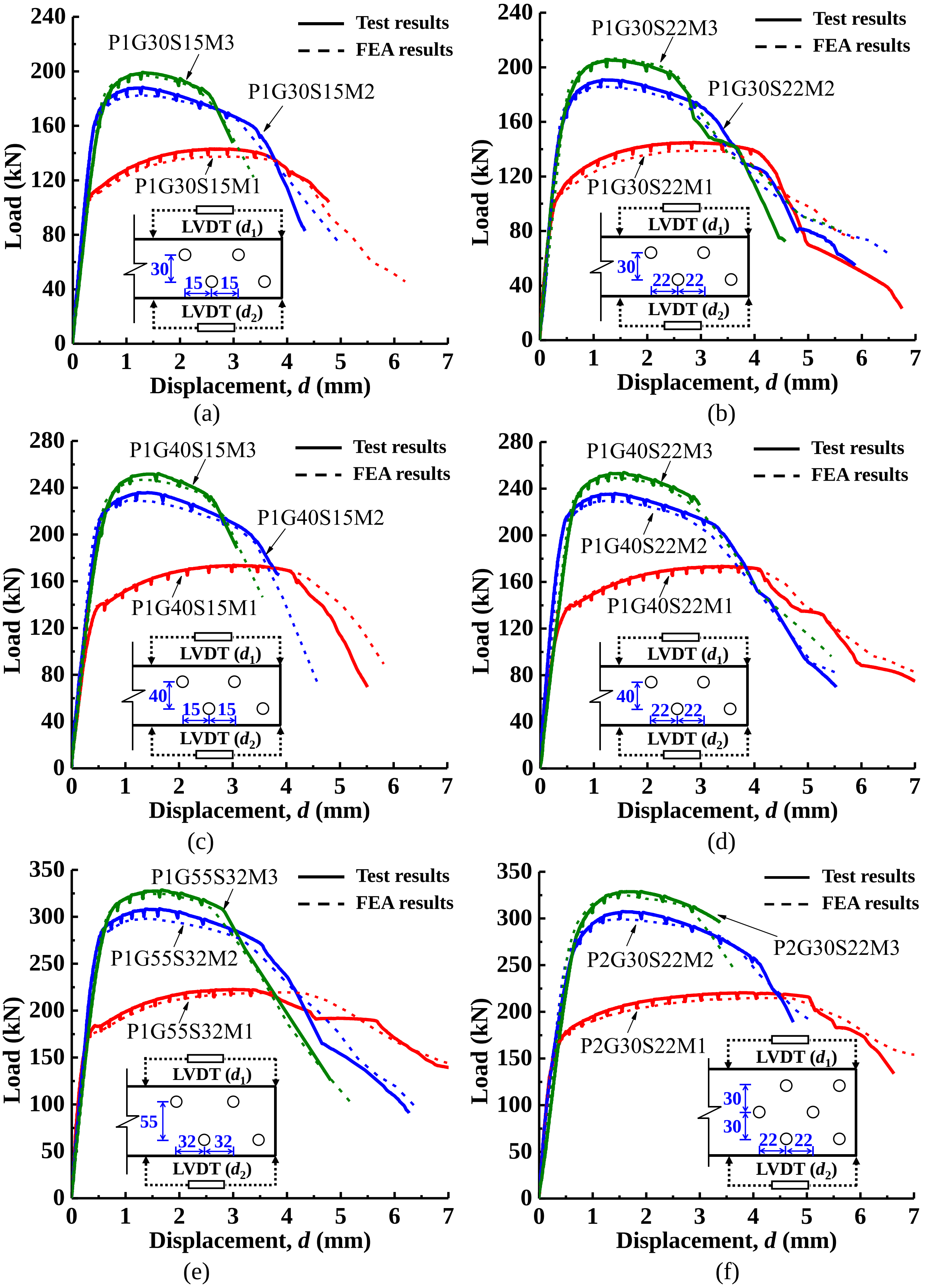

Fig. 6 Typical load-displacement curves

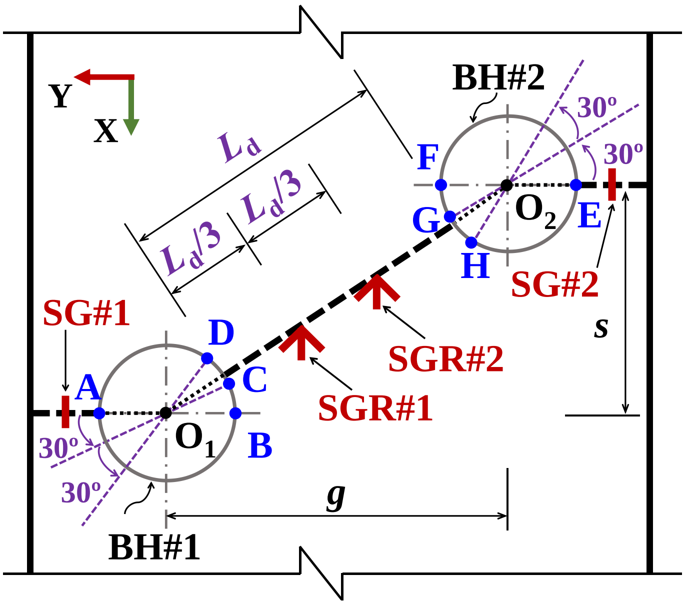

Fig. 7 Layout of the strain gauges and measurement points

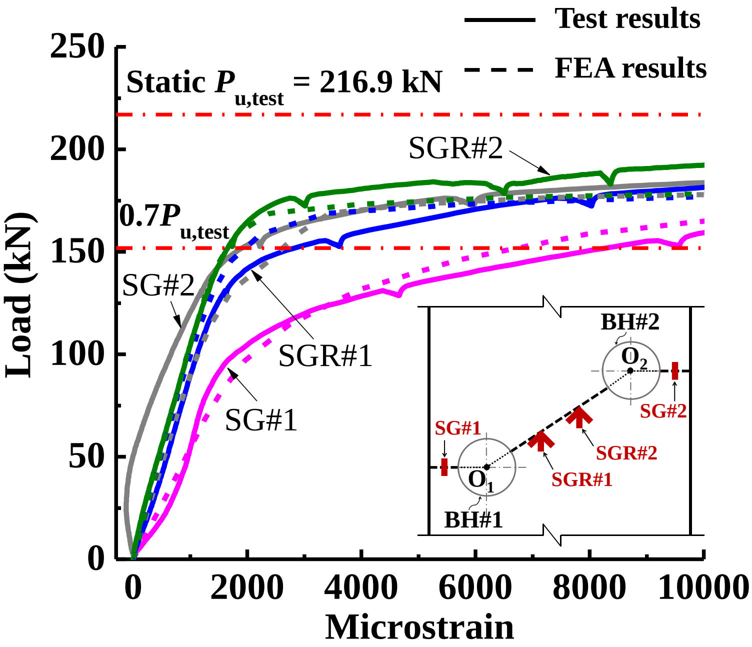

(a) P1G55S32M1

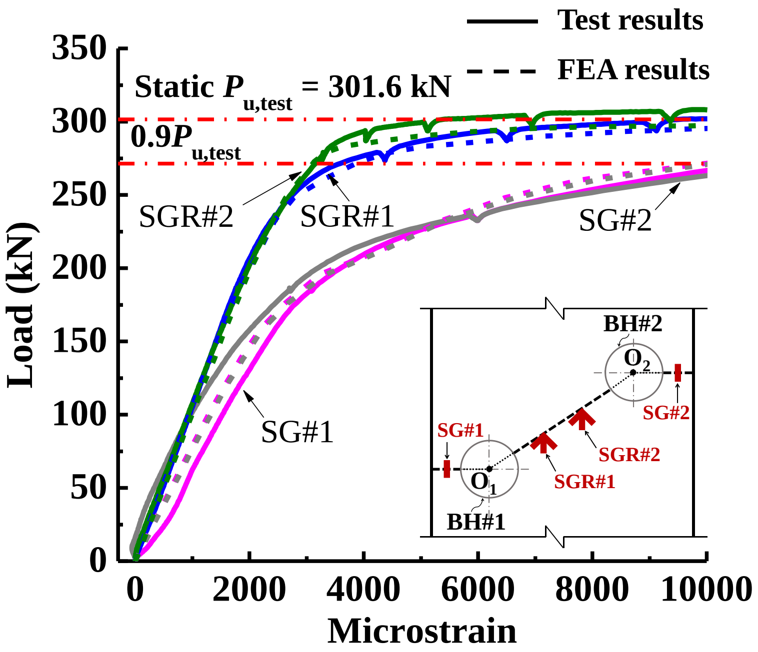

(b) P1G55S32M2

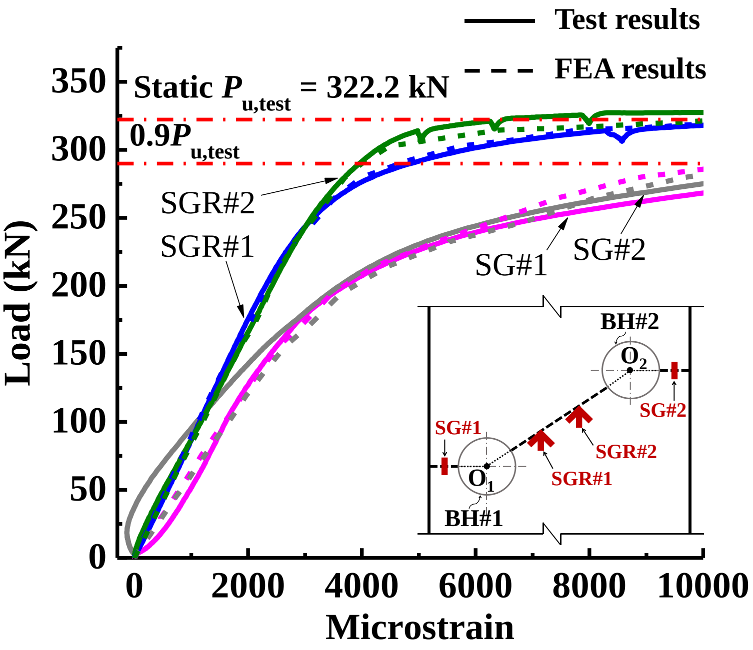

(c) P1G55S32M3

Fig. 8 Load-strain curves along the loading direction

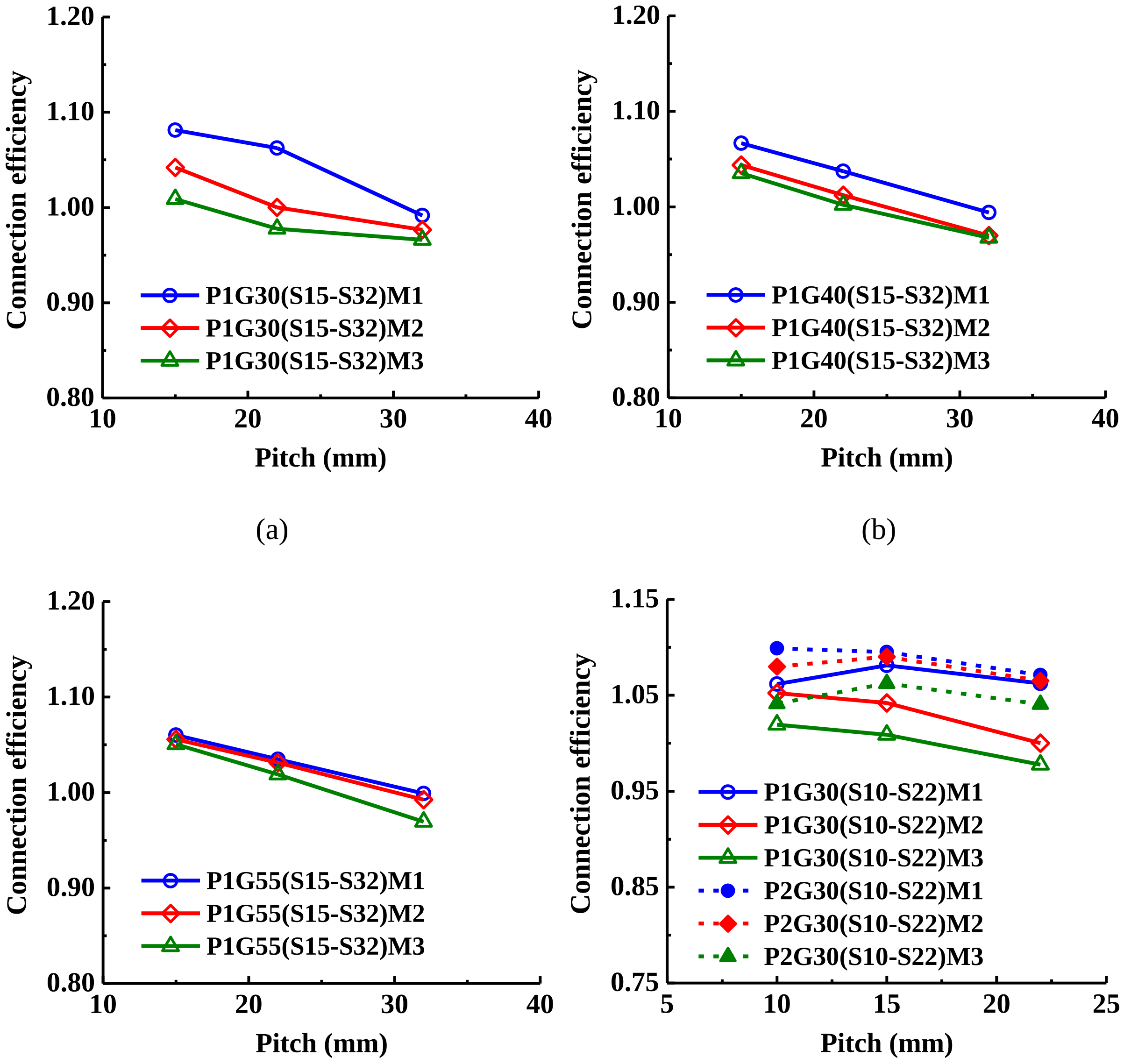

(a)

(b)

(c)

(d)

Fig. 9 Effect of bolt stagger on the connection efficiency

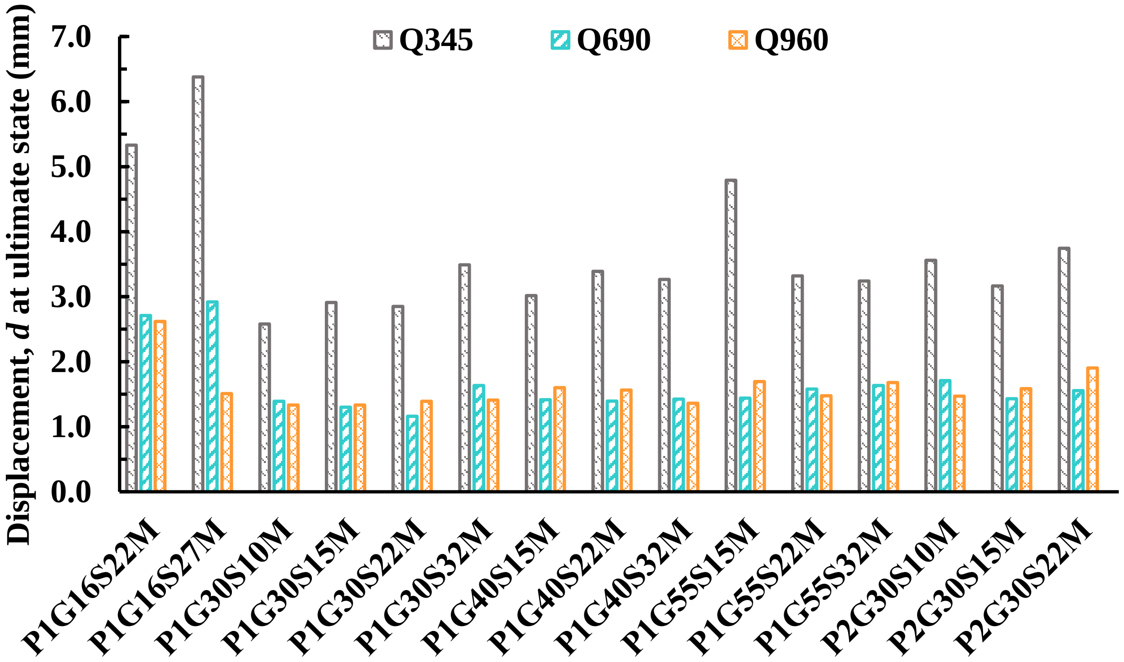

(a) Effect of steel grade on overall displacement

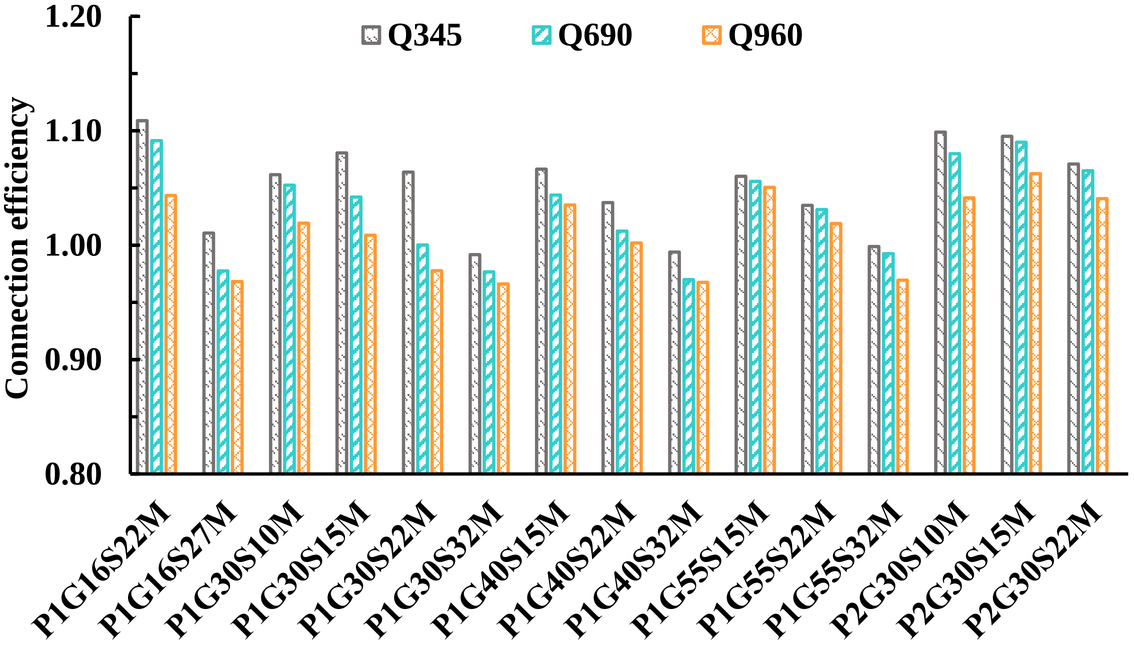

(b) Effect of steel grade on connection efficiency

Fig. 10 Effect of steel grade on overall displacement and connection efficiency

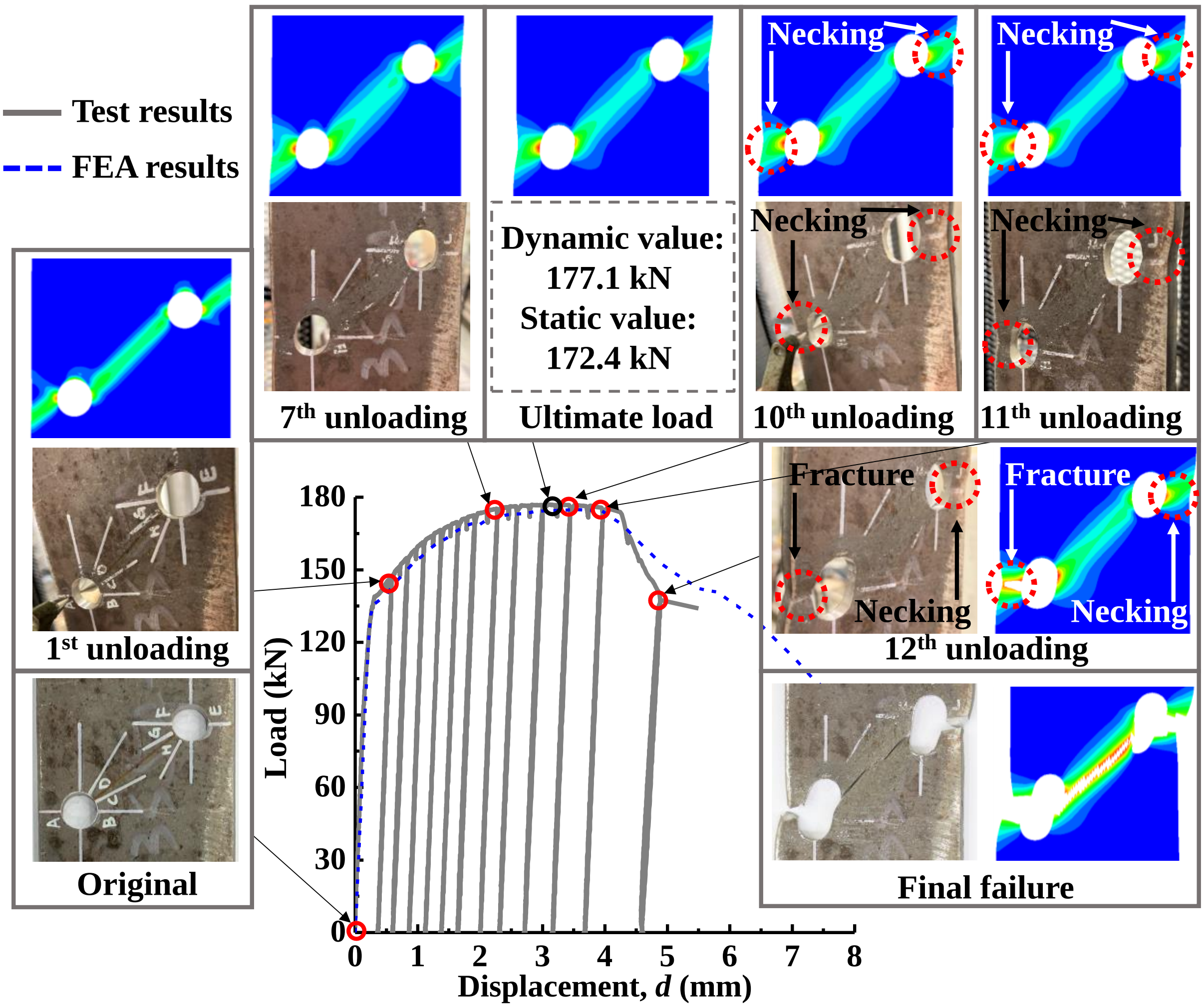

(a) Specimen P1G40S32M1

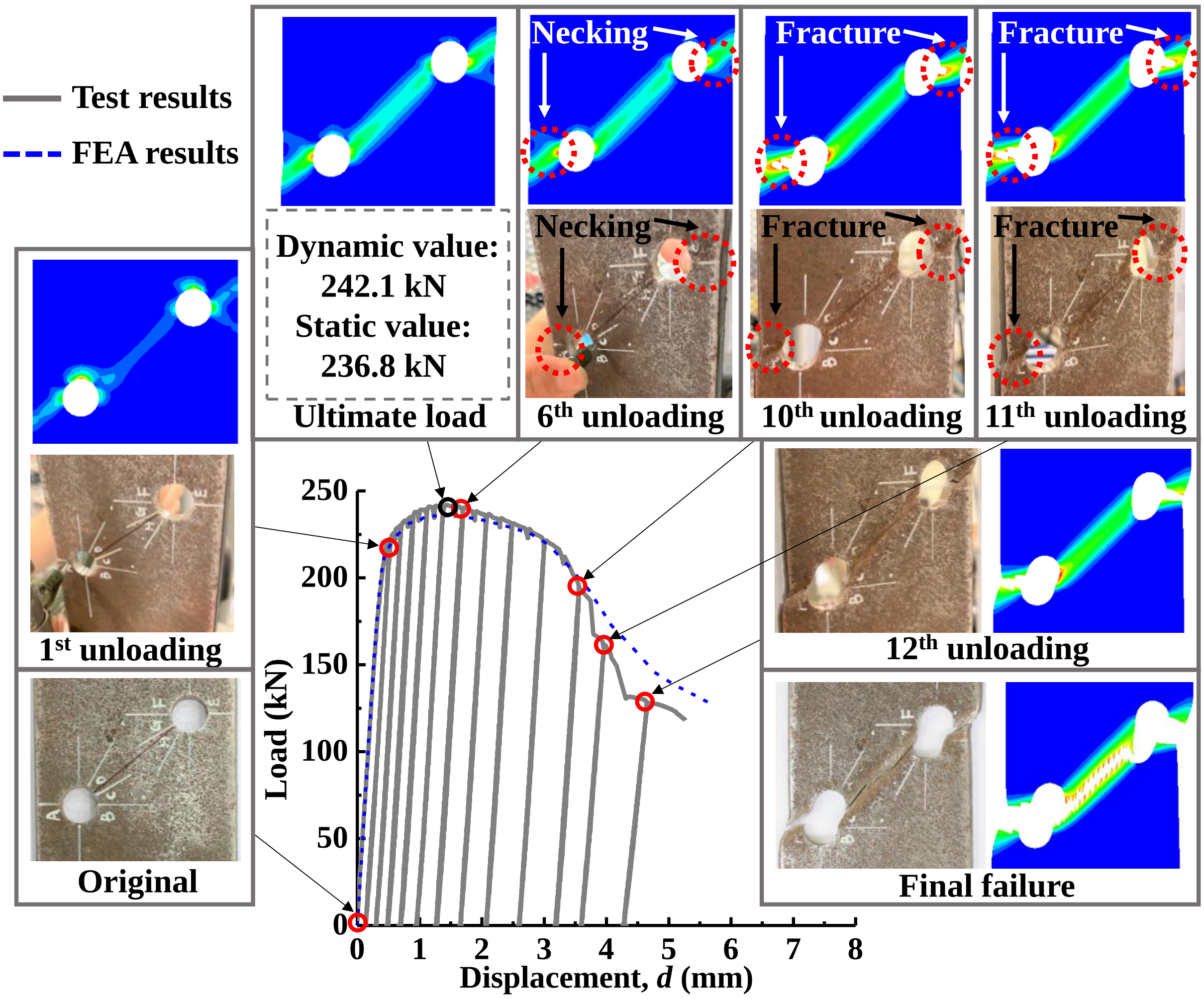

(b) Specimen P1G40S32M2

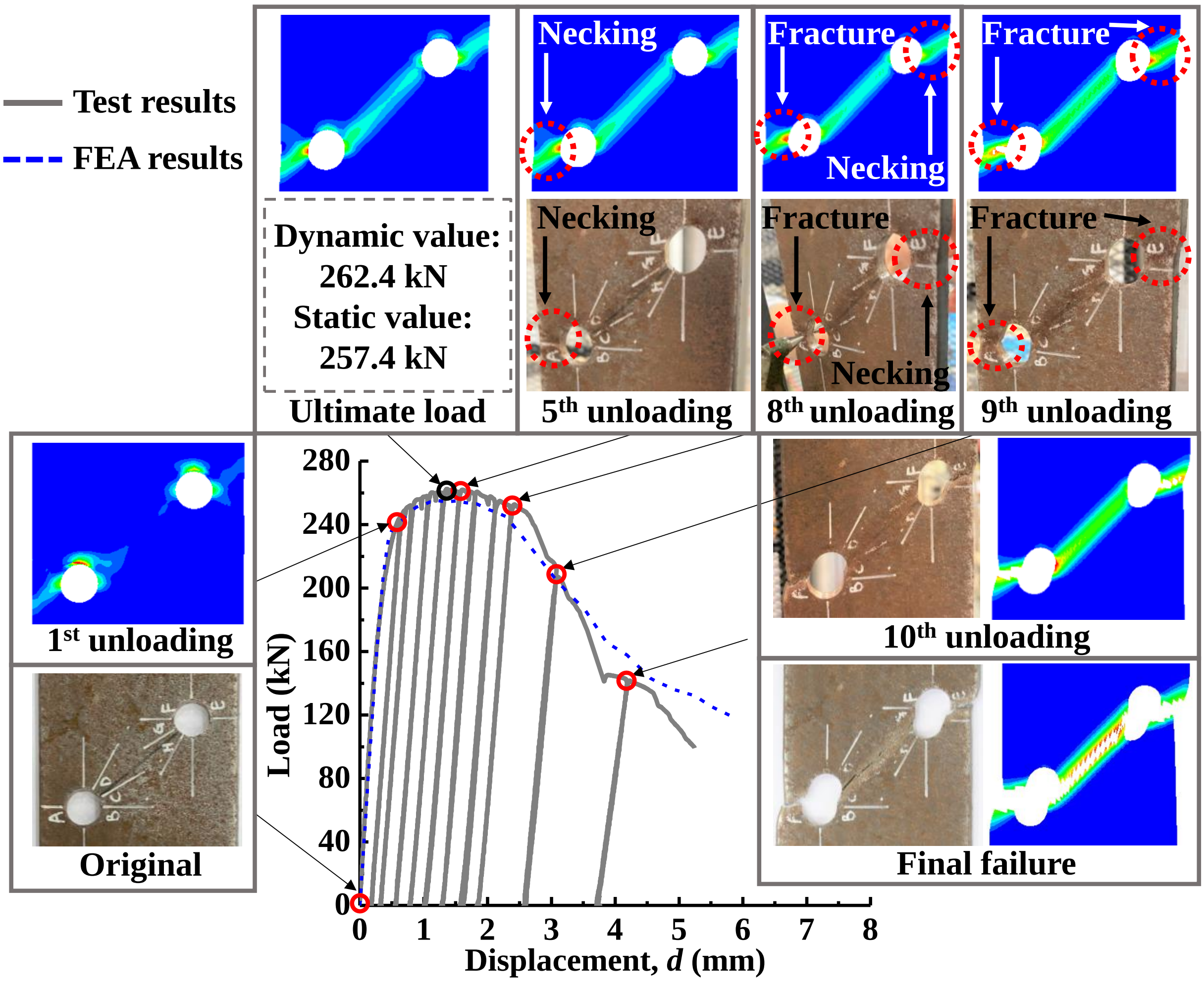

(c) Specimen P1G40S32M3

Fig. 11 Deformation process along the staggered net section

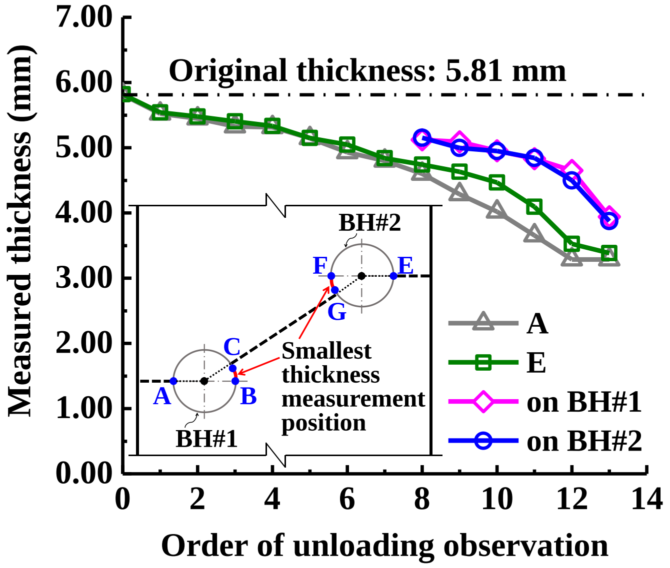

(a) Specimen P1G40S32M1

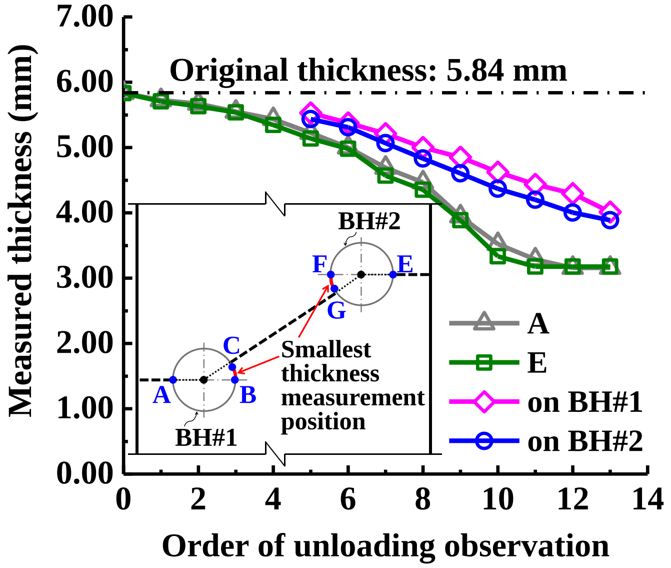

(b) Specimen P1G40S32M2

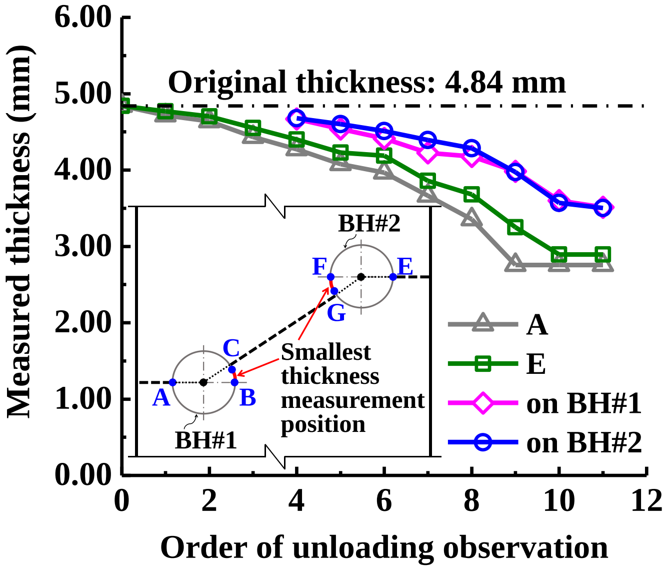

(c) Specimen P1G40S32M3

Fig. 12 Measured thickness at typical positions on the main plate

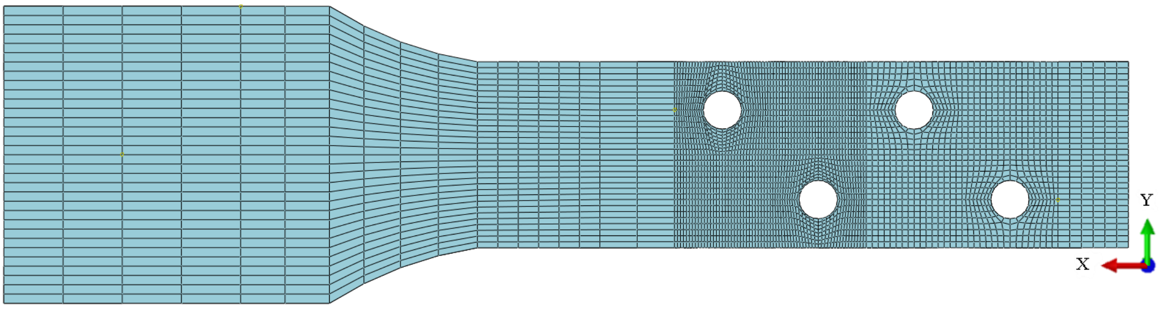

(a) Main Plate

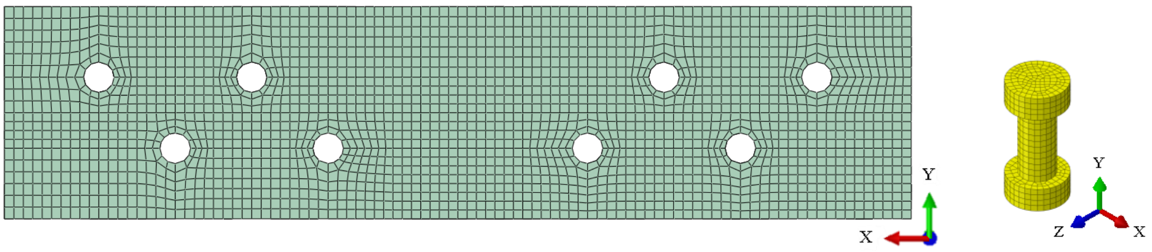

(b) Lap plate (c) Bolt

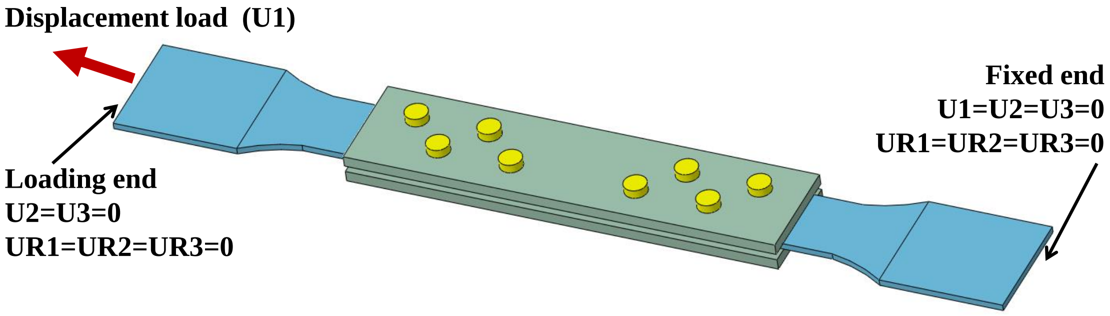

(d) Boundary conditions

Fig. 13 Typical FE model (Specimen P1G30S32M2)

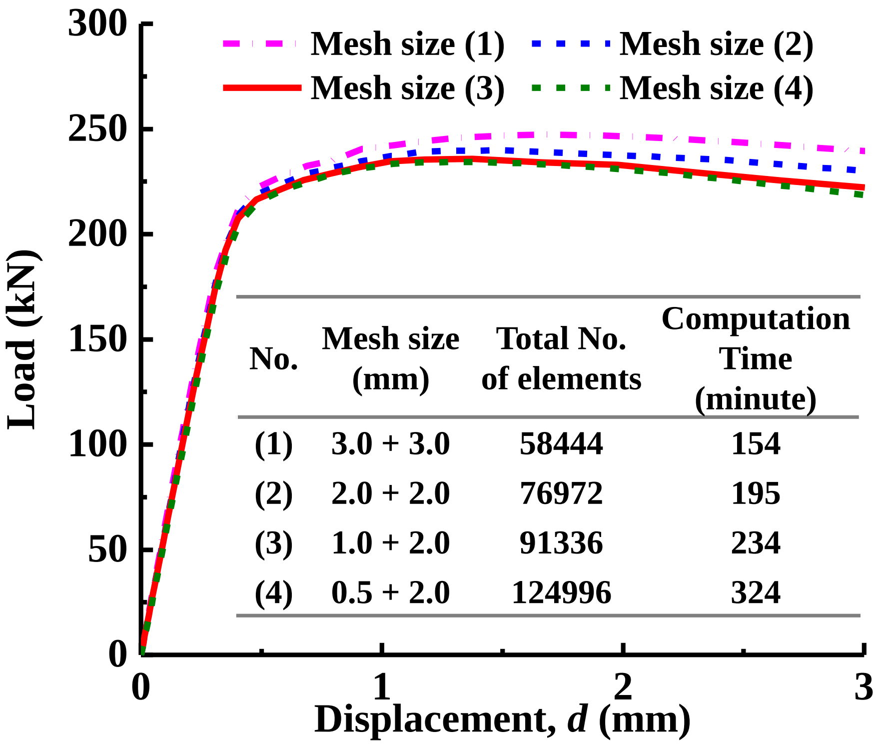

No.	Mesh size (mm)	Total No. of elements	Computation Time (minute)
(1)	3.0 + 3.0	58444	154
(2)	2.0 + 2.0	76972	195
(3)	1.0 + 2.0	91336	234
(4)	0.5 + 2.0	124996	324

Fig. 14 Results of the mesh convergence study (Specimen P1G40S32M2)

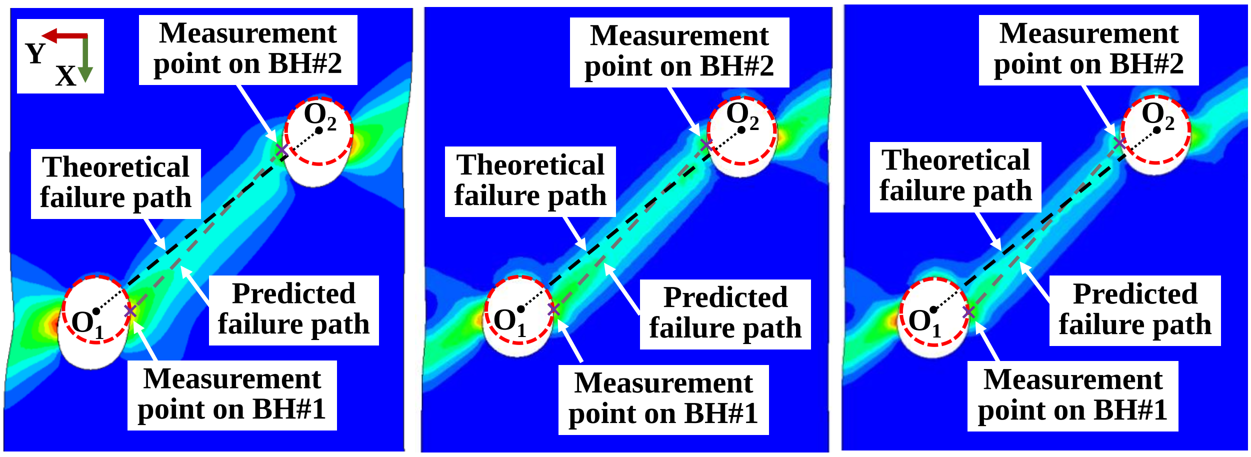

Position	The smallest plate thickness on inside edges of the bolt holes (mm)					
	t_{test}	t_{FE}	t_{test}	t_{FE}	t_{test}	t_{FE}
on BH#1	4.95	5.02	5.38	5.33	4.54	4.43
on BH#2	4.95	5.03	5.31	5.26	4.60	4.51

(a) P1G40S32M1 (*s*/*g*=0.8) (b) P1G40S32M2 (*s*/*g*=0.8) (c) P1G40S32M3 (*s*/*g*=0.8)

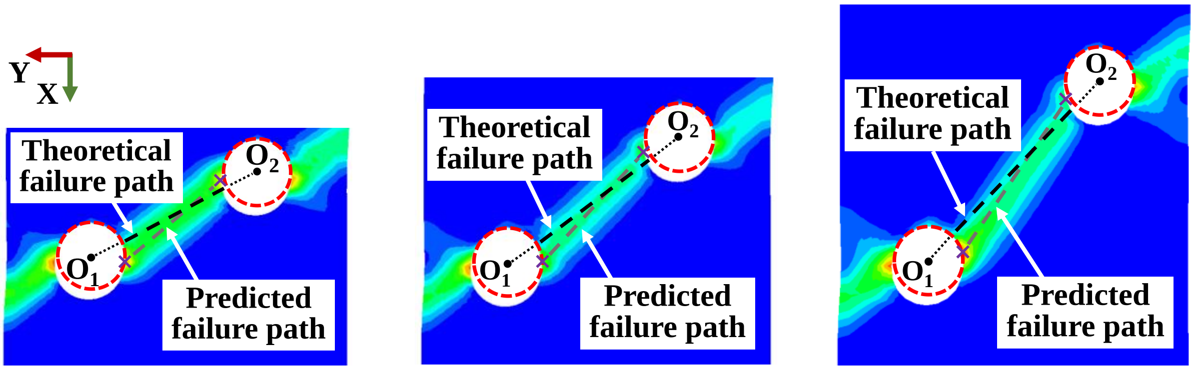

(d) P1G30S15M2 (*s*/*g*=0.5) (e) P1G30S22M2 (*s*/*g*=0.7) (f) P1G30S32M2 (*s*/*g*=1.1)

Fig. 15 Comparison of the position of theoretical and predicted failure paths between the staggered bolt holes at the ultimate state

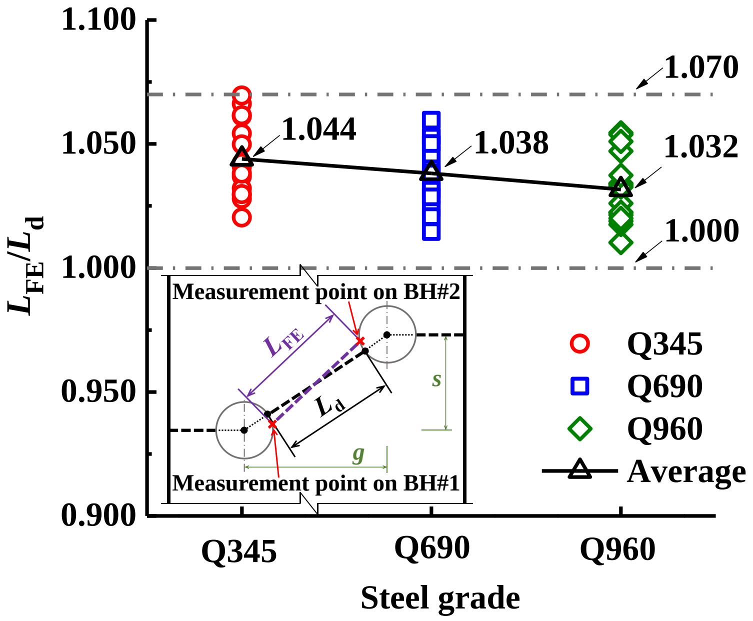

Fig. 16 Comparison of the length of predicted (L_{FE}) and theoretical (L_d) failure path between the staggered bolt holes

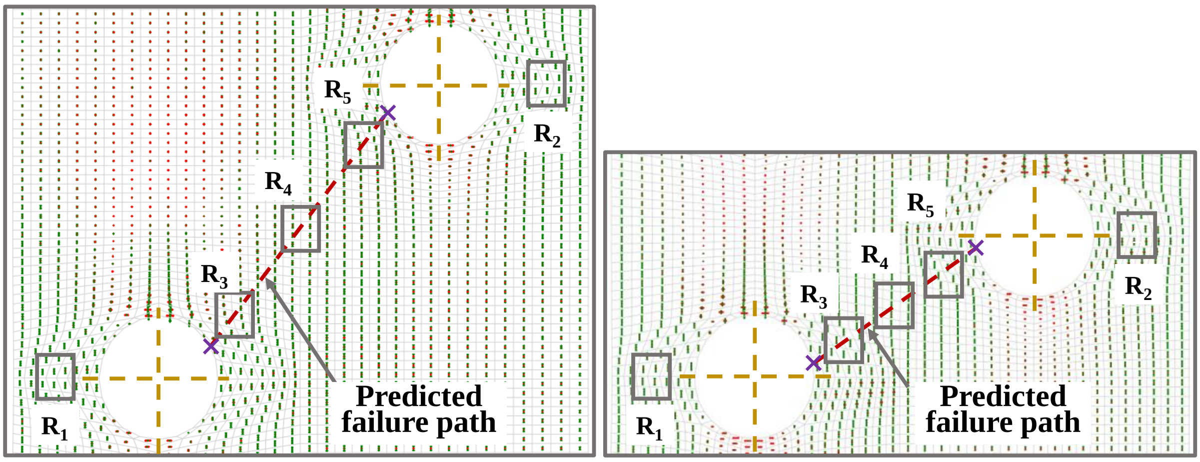

(a) Specimen P1G30S32M2 (*s/g*=1.1) (b) Specimen P1G30S15M2 (*s/g*=0.5)

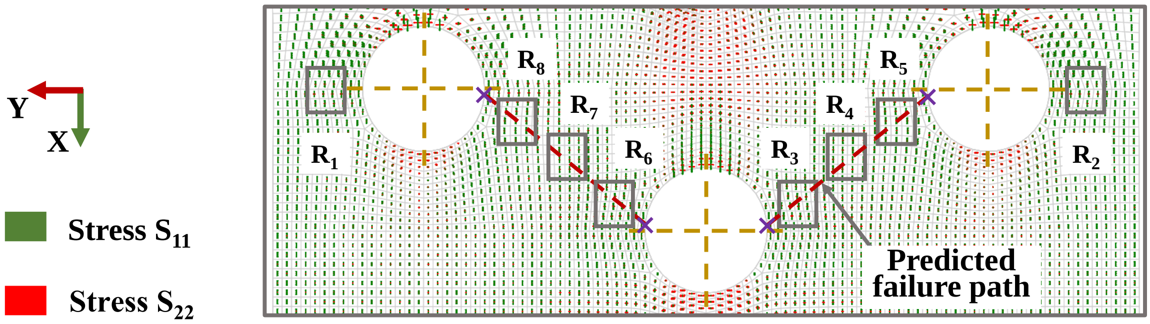

(c) Specimen P2G30S15M2 (*s/g*=0.5)

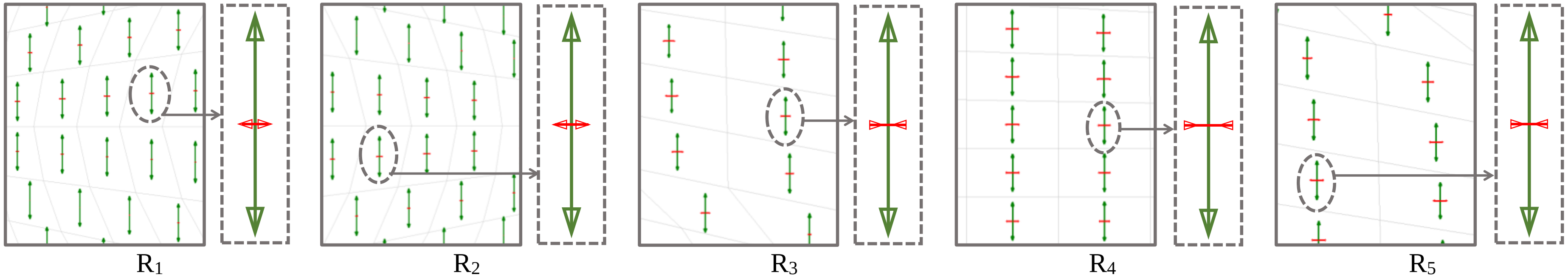

(d) The enlarged views of the stress plots on specimen P1G30S32M2 (s/g=1.1)

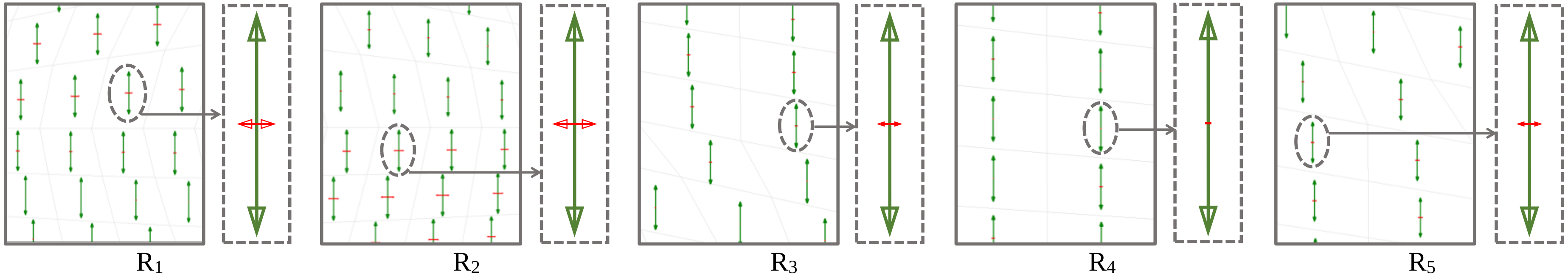

(e) The enlarged views of the stress plots on specimen P1G30S15M2 (s/g=0.5)

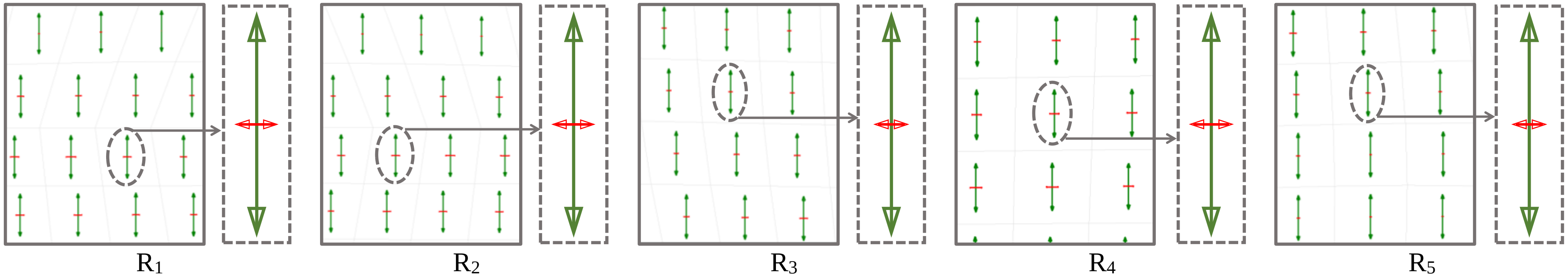

(f) The enlarged views of the stress plots on specimen P2G30S15M2 (s/g=0.5)

Fig. 17 Biaxial stress state across the staggered net section at loading stage $0.9P_{\mathrm{u,FEM}}$